ESA Climate Change Initiative (CCI+)

Essential Climate Variable (ECV)

Greenland_Ice_Sheet_cci+ (GIS_cci+)

Algorithm Theoretical Basis Document (ATBD) for CCI+ Phase 1

Prime & Science Lead: René Forsberg
DTU Space, Copenhagen, Denmark
rf@space.dtu.dk

Technical Officer: Marcus Engdahl
ESA ESRIN, Frascati, Italy
Marcus.Engdahl@esa.int

Consortium:
Asiaq Greenland Survey (ASIAQ)
DTU-Space, Department of Geodynamics (DTU-S)
DTU-Space, Department of Microwaves and Remote Sensing (DTU-N)
Danish Meteorological Institute (DMI)
Environmental Earth Observation IT GmbH (ENVEO)
Science [&] Technology AS (S&T)
Technische Universität Dresden (TUDr)
The Geological Survey of Denmark and Greenland (GEUS)
The Niels Bohr Institute (NBI)
University of Leeds, School of Earth and Environment (UL)

Signatures page

Prepared by	Jan Wuite Lead Author, ENVEO	[signature]	Date: 19 Oct. 2020
Issued by	Daniele Fantin, Project Manager, S[&]T	[signature]	Date: 5 May 2020
Checked by	Rene Forsberg Science Leader, DTU-S	[signature]	Date: 5 May 2020
Approved by	Marcus Engdahl ESA Technical Officer		Date:

Table of Contents

Change Log

Issue	Author	Affected Section	Change	Status
0.6	ENVEO	All	Draft version	
1.0	All	All	First version	
1.1	GEUS	6	Update on MFID	
1.2	DTU	2	Update on SEC	

Acronyms and Abbreviations

Acronyms	Explanation
ATBD	Algorithm Theoretical Basis Document
C3S	Copernicus Climate Change Service
CCI	Climate Change Initiative
CFL	Calving Front Location
CS2	CryoSat-2
CSR	Center for Space Research, University of Austin
DEM	Digital Elevation Model
DInSAR	Differential Interferometric Synthetic Aperture Radar
DMI	Danish Meteorological Institute
DTU-N	DTU Microwaves and Remote Sensing Group
DTU-S	DTU Geodynamics Group
E3UB	End-to-End ECV Uncertainty Budget
ECV	Essential Climate Variable
ENU	East North Up
ENVEO	ENVironmental Earth Observation GmbH
EO	Earth Observation
ESA	European Space Agency
GCOS	Global Climate Observation System
GCP	Ground Control Point
GEUS	Geological Survey of Denmark and Greenland
GFZ	Deutsche GeoForschungsZentrum
GIA	Glacial Isostatic Adjustment
GIS	Greenland Ice Sheet
GLL	Grounding Line Location
GMB	Gravimetry Mass Balance
GRACE(-FO)	The Gravity Recovery and Climate Experiment (Follow On)
IMBIE	Ice Sheet Mass Balance Inter-Comparison Exercise
InSAR	Interferometric Synthetic Aperture Radar
IPP	Interferometric Post-Processing
IV	Ice Velocity
JPL	NASA Jet Propulsion Laboratory
MAI	Multiple Aperture Interferometry
MEaSUREs	Making Earth System Data Records for Use in Research
MFID	Mass Flow Rate and Ice Discharge
NBI	Niels Bohr Institute, University of Copenhagen
NEGIS	North East Greenland Ice Stream
PROMICE	Danish Program for Monitoring of the Greenland Ice Sheet
RA	Radar Altimetry
RMS	Root Mean Square
S&T	Science and Technology AS

S2	Sentinel-2
SAR	Synthetic Aperture Radar
SEC	Surface Elevation Change
SLR	Satellite Laser Ranging
SMB	Surface Mass Balance
SOW	Statement of Work
TEC	Total Electron Content
TOA	Top of Atmosphere
TPROP	Technical Proposal
TUDr	Technische Universität Dresden
UL	University of Leeds
URD	User Requirement Document

1 Introduction

1.1 Purpose and Scope

This document contains the Algorithm Theoretical Basis for the Greenland_Ice_Sheet_cci (GIS_cci) project for CCI+ Phase 1, in accordance to contract and SoW (AD1 and AD2). The ATBD describes the scientific background and principle of the algorithms, their expected or known accuracy and performance, input and output data, as well as capabilities and limitations.

The ATBD for the Ice Sheets cci project (RD1) is used as a basis for this work. It describes the algorithms used to generate the ECV parameters 'Surface Elevation Change (SEC)', 'Ice Velocity (IV)', 'Calving Front Location (CFL)', 'Grounding Line Location (GLL)' and 'Gravimetric Mass Balance (GMB)'. The current document is a supplement to this, and the aim is to review and provide an update regarding improvements to existing algorithms, proposed for CCI+, and to document the theoretical basis for new algorithms implemented for Mass Flux and Ice Discharge (MFID) and Supraglacial Lake (SL).

1.2 Document Structure

This document is structured into an introductory chapter followed by 6 chapters focussed on the retrieval algorithms for each of the CCI+ parameters:

- Surface Elevation Change (SEC)
- Ice Velocity (IV-SAR)
- Ice Velocity (IV-Optical)
- Gravimetric Mass Balance (GMB)
- Mass Flow Rate and Ice Discharge (MFID)
- Supraglacial Lake (SL)

1.3 Applicable and Reference Documents

Table 1.1: List of Applicable Documents

No	Doc. Id	Doc. Title	Date	Issue/ Revision/ Version
AD1	ESA/Contract No. 4000126023/19/I-NB, and its Appendix 1	CCI+ PHASE 1 - NEW R&D ON CCI ECVS, for Greenland_Ice Sheet_cci	2019.04.01	
AD2	ESA-CCI-EOPS-PRGM-SOW-18-0118 Appendix 2 to contract.	Climate Change Initiative Extension (CCI+) Phase 1, New R&D on CCI ECVs Statement of Work	2018.05.31	Issue 1 Revision 6
AD3	ST-DTU-ESA-CCI-P2-GIS-TPROP	ESA Climate Change Initiative (CCI+) Greenland Ice Sheet (GIS) Essential Climate Variables Technical Proposal (TPROP)	2019.01.18	

Table 1.2: List of Reference Documents

No	Doc. Id	Doc. Title	Date	Issue/ Revision/ Version
RD1	ST-DTU-ESA-GISCCI+-PMP-001	ATBD for the Ice_Sheets_cci project of ESA's Climate Change Initiative	2017.08.28	3.2

Note: If not provided, the reference applies to the latest released Issue/Revision/Version

2 Surface Elevation Change

2.1 Introduction

Satellite altimetry provides estimates of ice sheet elevation changes through repeated measurements of ice sheet surface elevations. The technique has been employed to study both Greenland (e.g. Sørensen et al., 2018; Slater et al. 2019; IMBIE Team 2019) and Antarctica (e.g. IMBIE Team 2018, Schröder et al., 2019), and has the distinct advantage of being able to resolve the detailed pattern of mass imbalance, with frequent (up to monthly) temporal sampling. Radar altimetry, in particular, provides the longest continuous observational record of all geodetic techniques going back to 1991.

Altimeters using microwave frequencies are commonly referred to as radar altimetry. At these wavelengths the signal can penetrate cloud cover, making the measurements possible in all weather conditions. In addition, the use of microwaves enables measurements to be made independently from sunlight conditions. The satellites with altimeters onboard are placed in repeat orbits (covering a region of up to 1 km on either side of a nominal ground track) enabling systematic monitoring of the Earth.

Currently, several satellite altimeters are monitoring the cryosphere; CryoSat-2 with its unique SARIn technique/mode to map the margins of the ice sheet, Sentinel-3 that has the capability to using SAR at the ice sheet margin, and ICESat-2 which is a photon-counting altimeter operated by NASA. Within GIS CCI+ we currently include only RA data in our SEC solutions, but future data releases will also include ICESat-2.

Here, we describe the improvements that have been implemented to the GIS CCI processor [RD1] into the current GIS CCI+ processor.

2.2 Review of scientific background

We refer to the review of the scientific background already presented in (RD1) and describe here the relevant literature that has been published since (RD1).

The GIS CCI SEC processor and products have been presented in Sørensen et al., (2018), and the results were also included in the Mottram et al., (2019) paper. One of the main challenges of using RA to map SEC is the fact that the RA might penetrate into the snow and track subsurface layers. Simonsen & Sørensen, (2017) presented a thorough assessment of the best algorithms to be used for CryoSat-2 data in order to minimize the effect of changing penetration depth.

Slater, T. (2019b) has presented an alternative approach of separating surface and volume scattering in CryoSat-2 data which looks like a promising approach, although it requires analysis at RA waveform level, and within CCI+ we are currently making use of ESA L2 products only.

2.3 Algorithms

There are four algorithms implemented for SEC production in the GIS GCCI+ project.

1. TR (true repeat track)
2. XO (cross-over)
3. PF (Plane-fit)

These are already described in detail in (RD1) and in Sørensen et al., (2018) and will not be explained further here, but in Table 2.1 we indicate which algorithm is used for the creation of each 5-year SEC products. In previous versions also an AT (along track) algorithm was implemented, but in the current processor this has been replaced by the PF algorithm.

Table 2.1: Satellite data and algorithms used for each of the 5-yr SEC grids.

Period	Mission(s)	SEC algorithm
1992-1996	ERS-1 / ERS-2	TR / XO
1993-1997	ERS-1 / ERS-2	TR / XO
1994-1998	ERS-1 / ERS-2	TR / XO
1995-1999	ERS-1 / ERS-2	TR / XO
1996-2000	ERS-2	TR / XO
1997-2001	ERS-2	TR / XO
1998-2002	ERS-2	TR / XO
1999-2003	ERS-2 / Envisat	TR / XO
2000-2004	ERS-2 / Envisat	TR / XO
2001-2005	ERS-2 / Envisat	TR / XO
2002-2006	ERS-2 / Envisat	TR / XO
2003-2007	ERS-2 / Envisat	TR / XO
2004-2008	ERS-2 / Envisat	TR / XO
2005-2009	Envisat	TR / XO
2006-2010	Envisat	TR / XO
2007-2011	CryoSat-2 / Envisat	PF
2008-2012	CryoSat-2 / Envisat	PF
2009-2013	CryoSat-2 / Envisat	PF
2010-2014	CryoSat-2 / Envisat	PF
2011-2015	CryoSat-2 / Envisat	PF
2012-2016	CryoSat-2 / Envisat	PF
2013-2017	CryoSat-2 / Sentinel-3	PF
2014-2018	CryoSat-2 / Sentinel-3	PF
2015-2019	CryoSat-2 / Sentinel-3	PF

2.4 Input data and algorithm output

Figure 2.1 shows the processing lines for TR and PF (exemplified by CryoSat-2 input-data), two of the four, algorithms used to derive SEC.

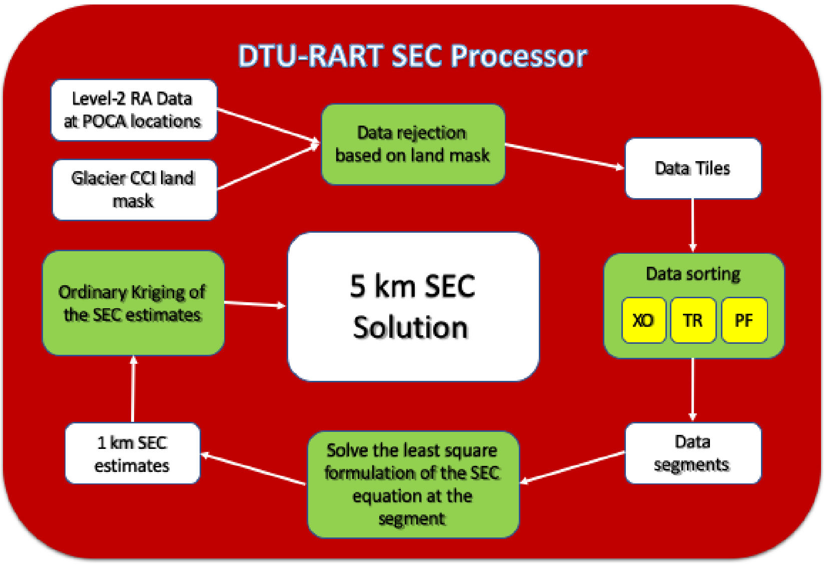

Figure 2.1: Workflow of the DTU-RART SEC processor.

2.4.1 Input data

The main improvements of the SEC processor are changes in the processor input data. These improvements are described below.

Ice mask

One of the improvements of the SEC processor within the CCI+ project is a change of one of the input datasets required. In the previous version as described in (RD1) the ice mask used in the processing line (See Figure 2.1), was generated from a digitized glacier outline that is now outdated. Therefore, we have changed the ice mask to be that of "gi_rgi05_003" (strongly connected glaciers + ice sheet) available through the Glacier CCI Database http://glaciers-cci.enveo.at/crdp2/index.html.

This data set is an update of gi_rgi05_001 and including only the peripheral glaciers and ice caps with connectivity level CL2 (strong connection to the ice sheet) and the updated ice sheet outline (Rastner et al., 2012).

This choice of using a new ice mask furthermore ensures consistency between CCI+ products as also the IV processor uses this ice mask.

RA data

The SEC processor utilizes more than 25 years of ESA radar altimetry observation, from six different satellites: ERS-1 and ERS-2, ENVISAT, CryoSat-2, and the two Sentinel-3 satellites A/B.

DEM

In the Greenland CCI SEC product, the GIMP-DEM was used as auxiliary DEM in the processing (RD1), for current CCI+ processing is the GIMP-DEM replaced by the newer ArcticDEM.

2.4.2 Algorithm Output

In the SEC products produced within GIS CCI to date, part of the margin of the Ice sheet was omitted due to the poor performance of the RA over these topographic regions. Figure 2.2 shows the full ice cover grid in yellow and the SEC product coverage in blue (slope less than 1.5 degrees). Now, we have chosen to provide full ice sheet coverage (main ice sheet + strongly connected glaciers as defined in glaciers CCI) (Rastner et al., 2012) for the SEC solutions. The errors are still large in these regions, but it will be up to the end-user to assess through the error grids that are provided with each SEC grid which grid cells to use.

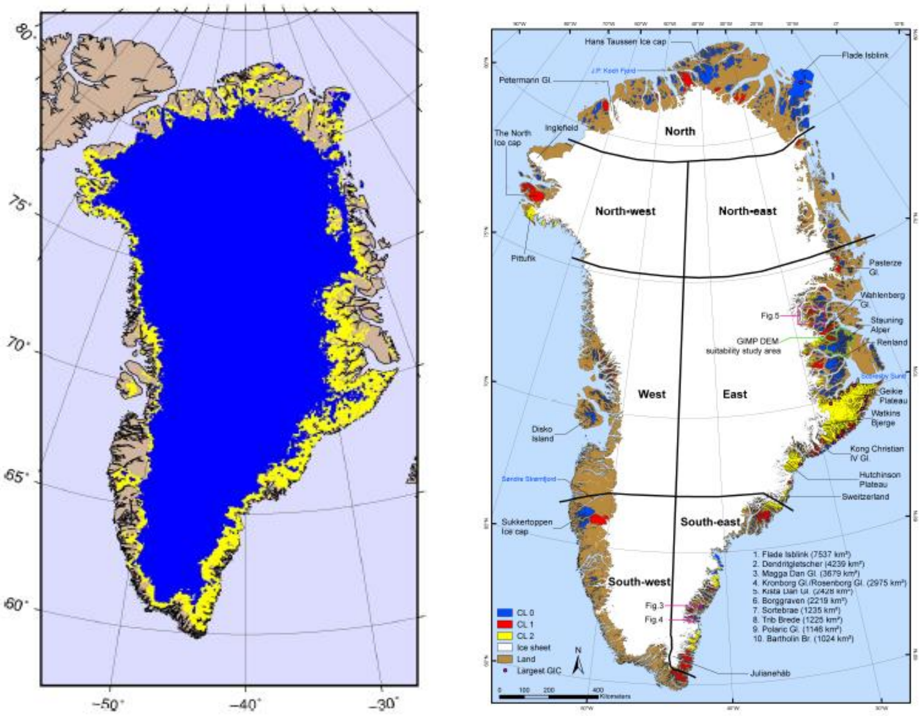

(a) (b)

Figure 2.2: (a) landcover grid showing all ice-covered area in yellow, and the coverage of previous pre-CryoSat-2 SEC solutions shown in blue. (b) ice mask from glaciers cci. For the SEC product we provide SEC over the ice sheet and strongly connected glaciers CL2. These are shown in white and yellow, respectively (Rastner et al., 2012).

We have changed the interpolation processing line from using least-squares collocation to using Kriging (Royle et al., 1981). Figure 2.3 thereby replaces Figure 2.7 in (RD1). Kriging is an advanced geostatistical predictor, that is efficient for generating surfaces from scattered points. The strength of Kriging is that it is based on an investigation of the spatial behaviour of the data based on a covariance analysis.

The primary reason for changing the interpolation scheme from Collocation to Kriging is that this will enable us to use more advanced versions like e.g. Kriging using external drift (using e.g. ice velocity as drift field) in future versions of our SEC products (Hudson, G., & Wackernagel, H. (1994)).

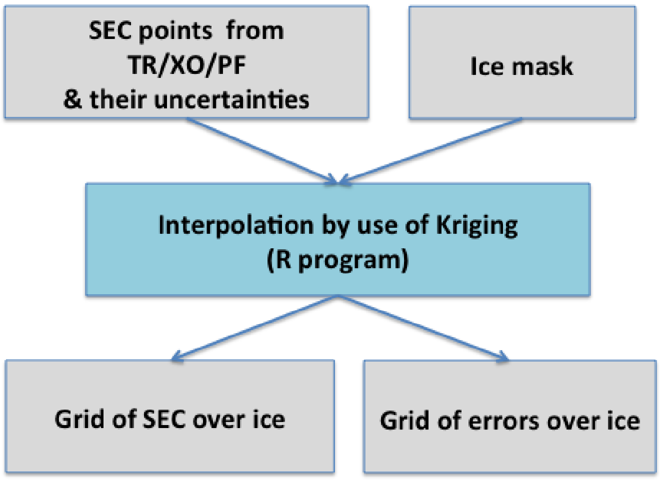

Figure 2.3: Schematic of the interpolation processing line.

2.5 Accuracy and performance

One benefit of using Kriging is the fact that it considers the error estimates of the point data and also creates a grid of errors along with the SEC output grid. At grid points close to the input data locations (satellite tracks and crossovers) the SEC error is controlled by the input error estimates, and it then increases with distance to the input data locations. This was also the case for the previous products derived using collocation, so the performance of using Kriging will be similar.

2.6 Capabilities and known limitations

We refer here to Sections 2.6.3, 2.6.4, and 2.6.5 of (RD1) for a summary of the known limitations. To these, we can add the current issues with the coastal tracking of the Sentinel-3 satellites. The current level-0 to level-1 processing are optimized for ocean-altimetry, this results in noisy radar-waveforms in the coastal areas of ice sheets, which again hampers the elevation retrievals. A dedicated land-ice processor is available which solves the issue, but yet not implemented operationally. When available operationally, we will switch from the ocean-processor to the land-ice processor.

2.7 References

Hudson, G., & Wackernagel, H. (1994). Mapping temperature using kriging with external drift: theory and an example from Scotland. International journal of Climatology, 14(1), 77-91.

IMBIE Team (2019). Mass balance of the Greenland ice sheet from 1992 to 2018. Nature. https://doi.org/10.1038/s41586-019-1855-2 ACCELERATED

IMBIE Team (2018). Mass balance of the Antarctic Ice Sheet from 1992 to 2017. Nature, 558(7709), 219–222. https://doi.org/10.1038/s41586-018-0179-y

Mottram, R., B Simonsen, S., Høyer Svendsen, S., Barletta, V. R., Sandberg Sørensen, L., Nagler, T., ... & Solgaard, A. (2019). An integrated view of Greenland ice sheet mass changes based on models and satellite observations. Remote Sensing, 11(12), 1407.

Rastner, P., Bolch, T., Mölg, N., Machguth, H., Le Bris, R., Paul, F. (2012): The first complete inventory of the local glaciers and ice caps on Greenland. The Cryosphere, 6, 1483-1495. (doi:10.5194/tc-6-1483-2012).

Royle, A. G., F. L. Clausen, and P. Frederiksen. "Practical Universal Kriging and Automatic Contouring." Geoprocessing 1: 377–394. 1981.

Schröder, L., Horwath, M., Dietrich, R., Helm, V., Van Den Broeke, M. R., & Ligtenberg, S. R. (2019). Four decades of Antarctic surface elevation changes from multi-mission satellite altimetry. The Cryosphere, 13(2), 427-449.

Simonsen, S. B., & Sørensen, L. S. (2017). Implications of changing scattering properties on Greenland ice sheet volume change from Cryosat-2 altimetry. Remote Sensing of Environment, 190, 207-216.

Slater, Thomas (2019) Mapping Ice Sheet Elevation and Elevation Change Using CryoSat-2 Radar Altimetry. PhD thesis, University of Leeds.

Slater, T., Shepherd, A., McMillan, M., Armitage, T. W., Otosaka, I., & Arthern, R. J. (2019b). Compensating Changes in the Penetration Depth of Pulse-Limited Radar Altimetry Over the Greenland Ice Sheet. IEEE Transactions on Geoscience and Remote Sensing.

Sørensen, L. S., Simonsen, S. B., Forsberg, R., Khvorostovsky, K., Meister, R., & Engdahl, M. E. (2018). 25 years of elevation changes of the Greenland Ice Sheet from ERS, Envisat, and CryoSat-2 radar

3 Ice Velocity (SAR)

3.1 Introduction

In Greenland_Ice_Sheet_cci+ the developments and further production for Ice Velocity (IV) build on the achievements of the GIS_cci Phase 1 and Phase 2 (2012-18). The major technical advancements emerging from GIS_cci were the development and implementation of an automatic system for generation of ice velocity maps from repeat pass Copernicus Sentinel-1 (S1) Synthetic Aperture Radar (SAR) using offset tracking (OT). The annual velocity maps and unprecedentedly dense IV time series of outlet glaciers provide essential information for studying temporal fluctuations and long-term trends and provide key input for ice dynamic and climate modelling and is continued within the C3S services on ice sheets.

In Greenland_Ice_Sheet_cci+ IV is derived from both SAR and optical data using combinations of coherent and incoherent OT and InSAR. The main technical development on SAR derived IV is the extension of the IV processor for supporting Sentinel-1 TOPS mode InSAR, using ascending and descending crossing orbit pairs acquired in Interferometric Wide (IW) swath mode. The development is expected to significantly improve the accuracy of the ice velocity, in particular in the slower moving areas in the interior of Greenland.

This chapter provides the Algorithm Theoretical Basis for IV, building on the ATBD of GIS_cci (RD1), and provides an overview, description and update of the scientific background, the IV retrieval algorithms, input and output data, expected accuracy and performance, and capabilities and known limitations.

3.2 Review of scientific background

To date, spaceborne methods for measuring ice velocity have focused on feature, offset and speckle tracking methods applied to optical and SAR sensors (Joughin et al, 2010; Nagler et al, 2015; Mouginot et al, 2017; Joughin et al, 2018). These methods have been extensively applied to Greenland and Antarctica ice sheets and have proven to be efficient for large-scale continuous monitoring (Nagler et al, 2015; Joughin et al, 2018). However, SAR offset-tracking methods are amplitude-based and do not exploit the full information provided by SAR images. Their accuracy is mostly controlled by the spatial resolution (i.e. pixel posting) of the sensor and reaches at best some meters per year.

In contrast, differential SAR interferometry can reach a precision of one to two orders of magnitude better than offset-tracking. Even though SAR interferometry has proved efficient for ice monitoring, it has been scarcely used for continuous monitoring of wide ice sheets. DInSAR requires measurements from crossing ascending and descending orbits in order to determine the different components of the velocity vector (Joughin, 1998; Gray, 2011). For this reason, DInSAR is in general applied to complement OT measurements (Joughin, 2002; Rignot et al, 2011; Mouginot et al, 2012), when data available only along ascending or descending tracks.

Before the launch of Sentinel-1A and B, such data were not systematically acquired and not always with a satisfactory temporal baseline. The unprecedented data set provided by Sentinel-1 satellites opens the possibility to improve the current IV measurements over Greenland by applying DInSAR in a systematic fashion. Recently, Mouginot et al, 2019 have released a comprehensive InSAR-based ice velocity map of Antarctica issued from more than 20-years of multi-sensor SAR acquisitions, which is the first example of this kind. To our knowledge, no comprehensive InSAR coverage of the Greenland Ice Sheet has been performed so far.

3.3 Algorithms

3.3.1 Differential SAR Interferometry

The interferometric phase ϕ difference between two SAR images acquired at different times is the sum of multiple components:

$$\phi = \phi_{flat} + \phi_{topo} + \phi_{displ} + \phi_{atm} + \phi_{iono} \quad \textbf{(Equation 3.1)}$$

where ϕ_{flat} is the flat-earth phase, ϕ_{topo} is the topographic phase, ϕ_{displ} is the phase due to ground displacement along the sensor line-of-sight (LOS), ϕ_{atm} is the atmospheric phase and ϕ_{iono} is the ionospheric phase. In order to estimate ice velocity, the displacement phase component must be isolated. This means that DInSAR processing includes removal of flat-earth and topography. Under the assumption that the atmosphere and the ionosphere are in a similar state for both acquisitions, the atmospheric and ionospheric components may be neglected.

The interferometric phase is computed as the argument of the product of the master image with the complex conjugate of the slave image. The result is a wrapped version of the absolute phase, with values ranging between $-\pi$ and π. The interferogram must be unwrapped in order to retrieve the absolute phase. However, phase unwrapping algorithms usually estimate the unwrapped phase of a pixel with respect to the phase of its neighbours. As a result, the unwrapped phase is shifted by an unknown amount with respect to the absolute phase. For this reason, the unwrapped phase must be further calibrated: the knowledge of points with zero velocity is used to determine the phase shift to be applied.

Once calibrated, the absolute phase must be converted into LOS velocity: LOS displacement is obtained by applying a $\frac{\lambda}{4\pi}$ conversion factor, with λ being the radar wavelength, and the velocity is calculated as the displacement per day, knowing the temporal baseline of the interferometric couple.

When interferometric processing is applied to a single geometry (i.e. to a given track, ascending or descending, with given heading and incidence angles), it only measures the displacement projected onto the line-of-sight. For calculating the 3-D velocity, LOS measurements from different geometries must be merged together.

Because interferometric measurements are prone to decorrelation, interferometry can only perform efficiently over ice bodies with stable conditions between the acquisitions: no melting, same type of snow surface, etc. Moreover, interferometry performs better on slow-moving areas: indeed, ice velocity can reach very large values (e.g. meters per day) causing important displacements even over a few days. Such displacements cannot be measured with interferometry as they result into aliased fringes in the interferogram that cannot be unwrapped.

3.3.2 Processing

The processing line is pictured in Figure 3.1. This processing line is designed for Sentinel-1 TOPSAR acquisitions (cf. IW – Interferometric Wide mode), but it can be easily modified to suit other sensors and acquisition modes.

In TOPSAR mode, the antenna is sequentially steered from the aft to the fore, so that the ground is not continuously scanned. The imaged area is scanned as 3 sub-swaths (or 5 in EW – Extended Wide mode), which are divided into slightly overlapping bursts. The interferometric processing, including coregistration, interferogram generation, phase flattening and topography removal is performed on each burst separately. The burst interferograms are then mosaicked at the debursting step.

The subsequent processing is performed at the debursted level. Once the interferogram generated, the phase must be unwrapped and calibrated. Afterwards, it can be converted into LOS velocity. In ENVEO implementation, the LOS velocity is also projected onto the horizontal plane. Images of horizontally projected LOS velocity are produced for different tracks and dates, and they are all geocoded on a common projection grid. Finally, these maps are used for inverting the system described below and for estimating the components of the horizontal velocity. The final product is a measurement of the east-west and north-south component.

In case of another acquisition mode than TOPSAR (e.g. Stripmap mode), the processing line is similar but the debursting step can be skipped as we are directly working with large-scale images. A short description of each module is provided below.

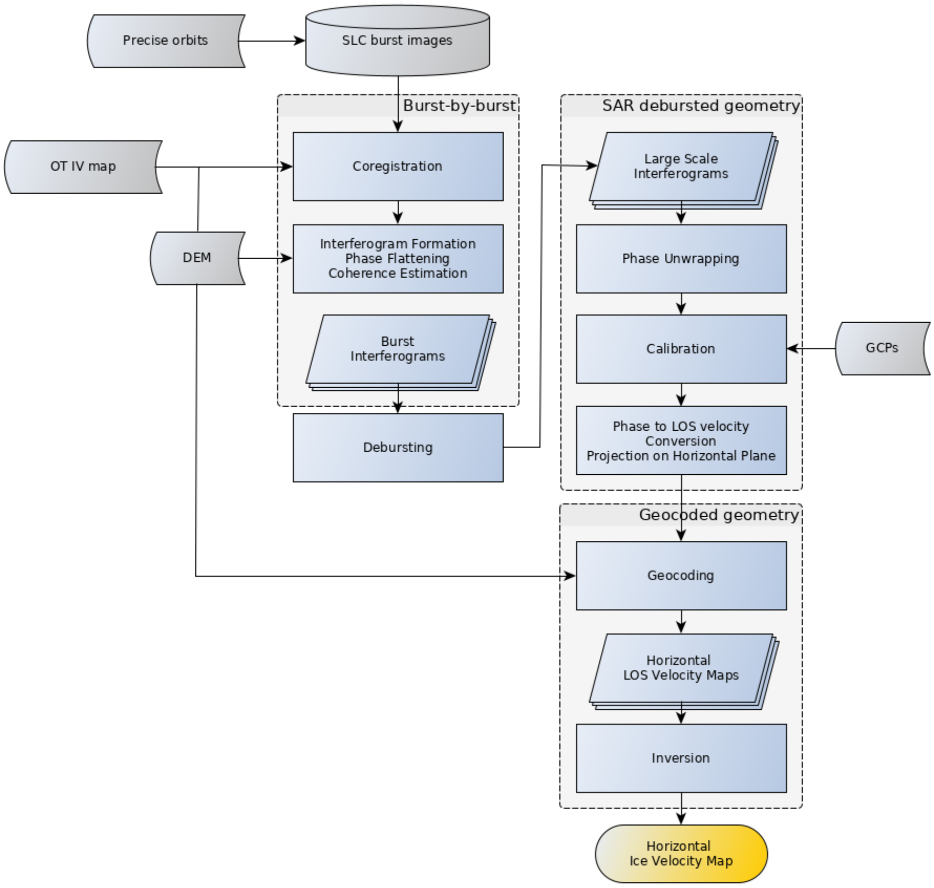

Figure 3.1: Differential interferometry processing for ice velocity (IV) map generation. The flowline is dedicated to Sentinel-1 TOPSAR acquisitions. SLC – Single-Look Complex. OT – Offset Tracking. LOS – Line-of-sight. GCP – Ground Control Point.

- **Coregistration:** coregistration is performed at the burst level. Precise orbits provided by ESA and a Digital Elevation Model (DEM) of the area are used to determine the shifts between the master and slave geometry. In TOPSAR mode, because of the steering of the antenna, the line-of-sight changes from one burst to the other at the overlapping area. In case of motion in the azimuth direction, the varying line-of-sight introduces phase discontinuities at burst overlap. We correct this effect by accounting for the average ice motion: using the IV map from Offset Tracking, we update the coregistration map with the local displacements between the master and slave acquisition dates. The coregistration module also includes the resampling step. For Sentinel-1 data, the steering of the antenna introduces a Doppler frequency variation in the azimuth direction. Therefore, the coregistration of Sentinel-1 images includes de-ramping and re-ramping of complex images in the azimuth direction respectively before and after interpolation.
- **Interferogram formation**: the interferometric phase is calculated for each master-slave burst pair. The flat-earth phase is estimated and removed. The topographic phase is estimated from an external DEM and subtract from the interferogram. The output is the wrapped displacement phase.
- **Debursting:** burst interferograms are mosaicked together using the range and azimuth time information of each pixel. Additional smoothing at the burst overlap can be performed to removed phase jumps due to changing orientation of the line-of-sight. These phase jumps are already significantly reduced by accounting for ice motion at the coregistration step.

- **Phase unwrapping:** phase unwrapping of very large interferograms can either be handled with SNAPHU, applying a tiling strategy (Chen and Zebker, 2002), or with an iterative least-square phase unwrapping.
- **Calibration:** calibration is usually performed by using zero-velocity ground control points (GCPs). However, zero velocity GCPs are not always available for all tracks covering the Greenland Ice Sheet. Therefore, we select low velocity as GCPs and perform calibration by adjusting their phase to the average velocity provided by the IV map from OT. For this purpose, the IV map has to be projected into SAR geometry, multiplied by the temporal baseline to yield the displacement, and converted into phase. A low order polynomial function is fitted to the difference between the IV phase from OT and InSAR of slow-moving points. If the polynomial order is 0, then calibration function consists in a simple constant shift. If the order is equal to 1 in azimuth and range directions, then the calibration function consists in a plane and accounts for possible orbits errors in the phase.
- **Phase-to-velocity conversion:** the calibrated absolute phase is converted into LOS velocity (i.e. displacement per day) by applying pixelwise the conversion factor $\frac{\lambda}{4\pi\Delta t}$, with λ being the radar wavelength and Δt the temporal baseline (usually provided in days). At this stage, the LOS velocity is further projected onto the horizontal plane. Projection onto the horizontal plane is obtained by dividing LOS velocity by the factor $\sin\theta$, where θ is the local incidence angle. Projection onto horizontal eases the final inversion, as all velocity vectors are already on a common plane and the system to be inverted only needs to account for heading angles.
- **Geocoding:** horizontally projected LOS velocity from all dates and tracks are geocoded on a common projection grid.
- **Inversion:** this step is meant to determine average horizontal velocity components. Provided that velocity measurements from at least two different geometry (i.e. two different heading angles) are available for a given point, the east-west and north-south velocity components can be determined. For this purpose, the system to be inverted is:

  $$\boldsymbol{V_{LOS} = AV} \qquad \textbf{(Equation 3.2)}$$

  where V_{LOS} is the N-dimensional vector of the measured LOS velocities projected on the horizontal plane, A is the matrix with dimensions N x 2 projecting the horizontal velocity on the LOS and V is the 2-dimensional vector of horizontal velocity components. Let us consider N horizontally projected LOS velocity measurements $v^H_{los_i}$. The index i refers to the geometry of acquisition and the corresponding heading angle ϕ_i. The system can be explicitly written as:

  $$\begin{bmatrix} v^H_{los_1} \\ v^H_{los_2} \\ \vdots \\ v^H_{los_N} \end{bmatrix} = \begin{bmatrix} \cos\phi_1 & \sin\phi_1 \\ \cos\phi_2 & \sin\phi_2 \\ \vdots & \vdots \\ \cos\phi_N & \sin\phi_N \end{bmatrix} \begin{bmatrix} v_E \\ v_N \end{bmatrix} \qquad \textbf{(Equation 3.3)}$$

  Where v_E and v_N are respectively the east and north components of the horizontal surface velocity. These components can be determined only where data with crossing orbits are available.

3.3.3 Remarks

The current processing is meant to determine horizontal ice velocity. Projecting the LOS velocity onto the local slope instead of the horizontal plane (cf. surface-parallel flow), 3-D surface velocity could be determined with a similar approach. It would however require slight changes into the current implementation of the flowline. Given that interferometry performs better over slow-moving ice bodies, such the interior of the Greenland Ice Sheet where the topography is rather flat, no significant difference is expected from the two approaches.

3.4 Input data and algorithm output

3.4.1 Input Data

The processing line is mainly dedicated to Sentinel-1 TOPSAR acquisitions. In this case, the input data are pairs of master and slave bursts in SLC format. In best cases, Sentinel-1 has a revisit cycle of 6 days. Given that ice motion can already cause very large displacements over 6 days, only short temporal baselines are selected (6 and 12 days). Moreover, the changing state of the ice during the melting season can cause decorrelation and prevent InSAR measurements. Therefore, we mainly focus on the winter season. Sentinel-1 IW and EW TOPS Mode SLC Products, as provided by ESA, consist of 3 or 5 sub-swaths, each consisting of a series of bursts, each burst has been processed as a separate SLC image. By importing Sentinel-1 SLC IW/EW SLC products into the software system each burst is extracted separately and the corresponding metadata information is stored in separate files. We especially take care to assign correct azimuth timing and slant-range timing for each burst, which is needed for debursting and for co-registering corresponding bursts of repeat pass acquisitions. Within the IV processor software an imported burst can be treated the same way as a frame of Stripmap Mode SAR data, except for the phase de-ramping needed during the resampling step.

Precise orbits of Sentinel-1 acquisitions are provided by ESA as independent products. These orbits have 5 cm accuracy in the along-track, across-track and vertical directions and are available 20 days after the acquisition.

The processor can be supplied with a digital elevation model in any supported projection (latitude-longitude, UTM, Polar Stereographic, etc.). The DEM is projected into the SAR geometry by the interferometric processor.

3.4.2 Algorithm output

The output product is a map of the east and north of components of horizontal ice velocity provided in meters per day. The velocity grid for a single image pair represents the average ice surface velocity over the respective repeat pass period. The generation of regional ice velocity maps requires the combination of results from several tracks. These maps form the input for further derived monthly and annually averaged maps.

3.5 Accuracy and performance

A detailed error analysis is outside the scope of this document, but the processing line has been tested over the North-East Greenland Ice Sheet (NEGIS). For this preliminary test, we focus on the period between January 1st and 13th, 2019. Interferometric pairs from tracks 10, 31, 54, 83, 89, 112 and 170 with 6-day temporal baseline have been selected and the processing line described above has been applied to each track. For visualization purpose, we converted the 2-D horizontal velocity into magnitude.

The result is shown in Figure 3.2, and it is compared with OT IV measurements. The agreement between both is rather good. Even with few data, IV magnitude is smoother for InSAR than for OT. Moreover, the IV map from InSAR processing does not suffer from streaks caused by ionosphere. In Figure 3.3 profiles of IV magnitude are provided for slow moving region and a faster moving one. For both regions, we observe good agreement between results from InSAR and OT.

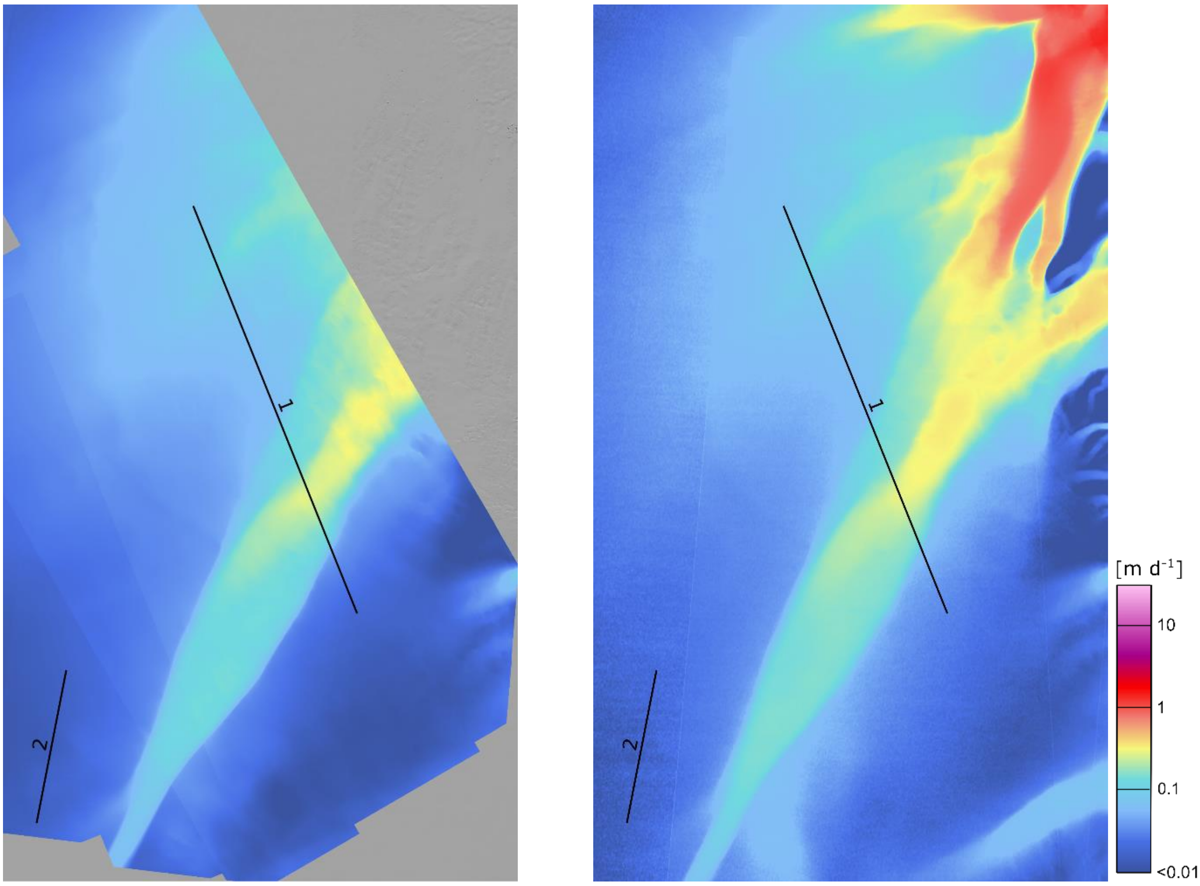

Figure 3.2: Maps of horizontal ice velocity magnitude over the North-East Greenland Ice Sheet. Left: From InSAR processing of Sentinel-1 6-day pairs acquired between 1st January and 13th January 2019. Right: From all OT measurements between 2014 – 2019. The same colour is used for both maps. Black lines indicate where velocity profiles are extracted.

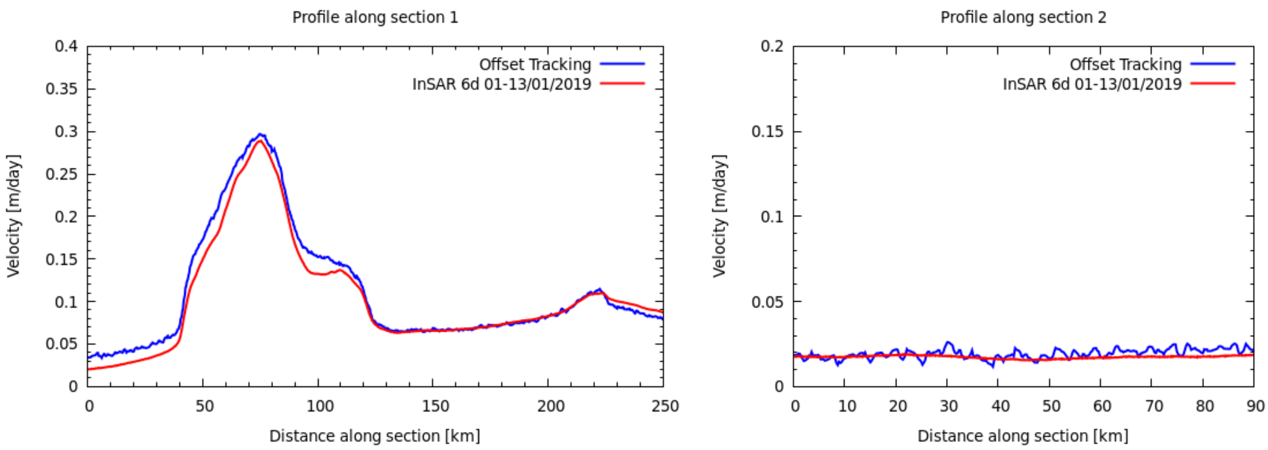

Figure 3.3: Comparison between IV measurements from InSAR and OT. Left: Velocity magnitude along section 1. Right Velocity magnitude along section 2. Sections 1 and 2 are indicated in Figure 3.2.

3.6 Capabilities and known limitations

Compared to the Offset Tracking approach that yields at best an accuracy of some tens of centimetres, DInSAR has the ability to estimate ground displacements with an accuracy better than a centimetre. However, InSAR performance for measuring ice motion is limited by a number of factors. The main limitations are:

- Ionosphere: at high latitude, the total electron content (TEC) of the ionosphere is very likely to vary (both in space and time) between two acquisitions. Different TEC introduce a phase delay related to the path travelled through ionosphere, which can bias or mask the ice motion signal.
- Change in snow conditions: if snow surface undergoes change such as melting or snowfall, the change in the surface state can cause decorrelation. For this reason, DInSAR shows better performance during the wintertime, during which snow conditions are more stable.
- Fast-moving areas: large displacements cause aliasing or decorrelation in interferograms. For this reason, fast-moving ice areas cannot be efficiently covered by Sentinel-1 data with 6-day revisit time.

3.7 References

Chen, C. W. and Zebker, H. A. (2002), Phase unwrapping for large SAR interferograms: Statistical segmentation and generalized network models”,' IEEE Transactions on Geoscience and Remote Sensing, vol. 40, pp. 1709-1719.

Gray, L. (2011), Using multiple RADARSAT InSAR pairs to estimate a full three-dimensional solution for glacial ice movement. Geophysical Research Letters, 38(5).

Joughin, I., Kwok, R. and Fahnestock, M.A. (1998) Interferometric estimation of three-dimensional ice-flow using ascending and descending passes. IEEE Trans. Geosc. and Remote Sens., 36(1), 25-37.

Joughin, I. (2002). Ice-sheet velocity mapping: a combined interferometric and speckle-tracking approach. Annals of Glaciology, 34, 195-201.

Joughin, I., Smith, B. E., Howat, I. M., Scambos, T. and Moon, T. (2010). Greenland flow variability from ice-sheet-wide velocity mapping. Journal of Glaciology, 56(197), 415–430. doi:10.3189/002214310792447734

Joughin, I., Smith, B. E. and Howat, I. (2018), Greenland Ice Mapping Project: ice flow velocity variation at sub-monthly to decadal timescales, The Cryosphere, 12, 2211–2227, https://doi.org/10.5194/tc-12-2211-2018, 2018.

Mouginot, J., Rignot, E. and Scheuchl, B. (2019). Continent-wide, interferometric SAR phase, mapping of Antarctic ice velocity. Geophysical Research Letters. doi:10.1029/2019gl083826

Mouginot, J., Rignot, E., Scheuchl, B. and Millan, R. (2017), Comprehensive Annual Ice Sheet Velocity Mapping Using Landsat-8, Sentinel-1, and RADARSAT-2 Data. Remote Sens. 2017, 9, 364.

Mouginot, J., Scheuchl, B. and Rignot, E. (2012), Mapping of Ice Motion in Antarctica Using Synthetic-Aperture Radar Data. Remote Sens. 2012, 4, 2753-2767.

Nagler, T., Rott, H., Hetzenecker, M., Wuite, J. and Potin, P. (2015), The Sentinel-1 Mission: New Opportunities for Ice Sheet Observations. Remote Sens. 2015, 7, 9371-9389.

Rignot, E., Mouginot, J. and Scheuchl, B. (2011), Ice flow of the Antarctic Ice Sheet. Science, 333(6048), 1427–1430. https://doi.org/10.1126/science.1208336

4 Ice Velocity (Optical)

4.1 Introduction

Based on the URD, the IV algorithms must be able to generate ice-sheet maps of mean-seasonal velocities as well as time-series of velocity measurements. The term velocity should be understood as "velocity vector", since users require all its components to be measured. These and other requirements are summarized in Table 4.1, where also the GCOS requirements are reported for convenience. The core measurement techniques for IV are quite well established and the one used for the retrieval of the IV from optical imagery is shortly described in section 4.3. In order to meet the requirements listed in Table 4.1, an algorithm combining these core-techniques is required.

Table 4.1: Overview of IV requirements

Parameter	URD	GCOS
Velocity components	Cartesian (ENU)	-
Spatial coverage	Whole ice-sheet*	-
Minimum spatial resolution	100m-1km	100 m
Optimum spatial resolution	50-100m	
Minimum temporal resolution	Annual	Monthly
Optimum temporal resolution	Monthly	-
Minimum accuracy	30 m/y	10 m/y

* Note: Optical IV ECV is produced for 9 large outlet glaciers only. Indeed, a large amount of science users are interested in these outlet glaciers because they represent the outlet conduits for the majority of ice sheet mass loss.

4.2 Review of scientific background

Space-borne IV measurements are currently carried out with SAR or with optical sensors. For the calculation of optical IV, measurement techniques based on optical imagery are offset-based (speckle-, feature- and coherence-tracking).

The main characteristics of offset tracking methods, and particularly feature-tracking one, which is the one used for the production of the CCI Optical IV ECV, is described in the following sub-sections.

4.3 Algorithm

Three methods are commonly used to derive ice velocity from satellite image data:

1. Differential SAR Interferometry DInSAR
2. Multiple Aperture Interferometry (MAI)
3. Offset Tracking

The optical IV ECV produced within the CCI project is based on the offset tracking method, and more specifically feature-tracking. The term offset tracking refers to a family of methods, which includes speckle-tracking (Gray et al. 2001; Joughin, 2002), coherence-tracking (Derauw, 1999) and feature-tracking (Lucchitta et al., 1995; Michel and Rignot, 1999; De Lange et al., 2007). The same approach is applicable to both SAR and optical images. SAR data have the advantage of an active sensor that is not affected by solar illumination (day/night) or cloud coverage, two aspects particularly relevant at high latitudes. IV retrieval from high resolution optical data allow to fill gaps in SAR IV products during summer in areas with surface melt, in particular along the margins.

Offset tracking methods estimate the spatially varying misalignment (offset) of a pair of optical images, due to surface motion, and provide velocity measurements in sensor geometry (horizontal for optical).

The feature-tracking algorithm used to calculate optical IV CCI ECV is based on IMCORR (Fahnestock et al. 1992; Scambos et al. 1992). The algorithm determines offsets by cross-correlating small subscenes (called "chips" or "patches") from two input images. The program uses a fast Fourier transform - based version of a normalized cross-covariance method (Berenstein, 1983).

At each of the grid points, the algorithm calculates a correlation index for every location at which the reference chip will entirely fit within the search chip. IMCORR takes the correlation values in the vicinity of the best integer-pixel match and interpolates a peak correlation location to sub-pixel precision, returning the displacements required to best match the chip pairs. The size of both search and reference subscenes is adjustable, ranging from 16x16 to 256x256 pixels (128x128 pixels for the reference one).

In the optical IV processing chain, the offset technique described above generates the offsets required to best match the reference chip pixels with the search chip pixels. Those offsets are finally converted in the velocity components towards the easting (x) and northing (y) directions on a polar stereographic grid, denoted as V_e and V_n respectively in Figure 4.1.

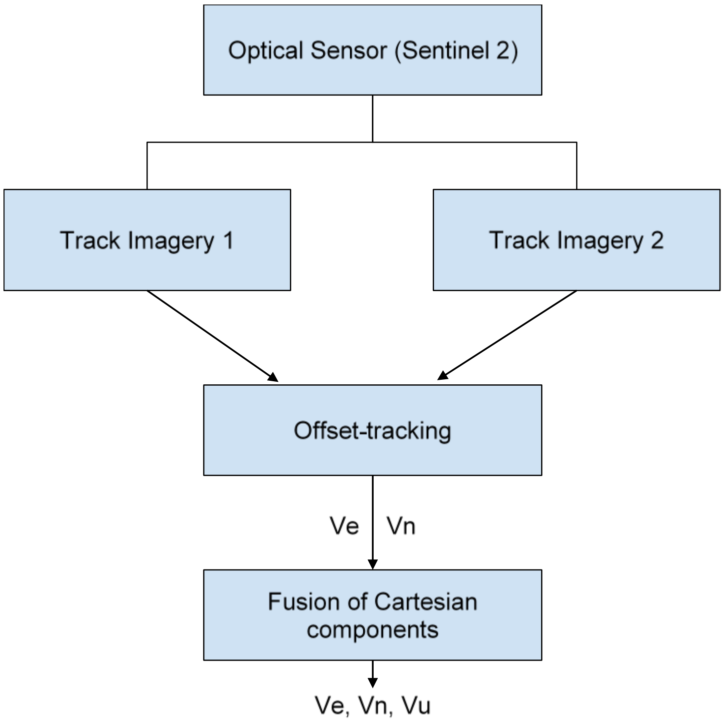

Figure 4.1: Overview of optical IV algorithm

4.4 Input data and algorithm output

All offset tracking methods require one image pair acquired from the same ground track. For the optical IV, this image is a high-resolution optical data (Sentinel 2). While setting up the processing chain for generating the optical IV ECV, several parameters can be fine-tuned, including grid size of the input data sets, search cells size (used to find correlating reference chips) and the size of the reference cells (reference cell to be found in the search subscene). Pre-set offsets of search cell centre may also be specified.

The reference image has the smaller, reference subscene derived from it, at regular grid spacings. These subscenes are then compared to larger search subscenes derived from the search image.

The outputs are the locations of the grid centres (in sensor coordinates) for the reference chips and the horizontal displacement (in 2 dimensions, x and y) between the two input images.

The inputs and outputs of the algorithm are listed in Table 4.2:

Table 4.2: main inputs and outputs of the optical IV algorithm

	Name	Description
Input	Data set 1	Reference image (grid)
	Data set 2	Search image (grid)
	Search chip size	Search subscenes size in pixels
	Reference chip size	Reference subscenes size in pixels
	Grid spacing	Grid spacing in pixels
Output	x displacement	Displacement along the x coordinate (in sensor geometry) between correlated points
	y displacement	Displacement along the y coordinate (in sensor geometry) between correlated points
	Strength of correlation	Strength of correlation between correlated points
	Correlated Points	Correlated points with displacement and correlation information
	x error	x estimated error in pixels
	y error	y estimated error in pixels

4.5 Accuracy and performance

Feature-tracking accuracies are approximately 2 times worse than algorithms based on other types of methods, as for example speckle-tracking (De Lange et al., 2007). They are not affected by low or absence of coherence, and they do not have a limit on the maximum measurable velocity magnitude, at least when applied to the range of velocities of the Greenland ice-sheets (< 13 km/y).

It is also important to highlight that the presence of features in the input imagery is essential for feature-tracking. This is often not the case in the interior of the Greenland ice-sheet. As consequence, this type of algorithm is applied to optical imagery mostly along the margins.

The objective of pre-processing steps is therefore to enhance surface features of the ice, with as little noise, sensor effects, and solar illumination effects as possible. As an example, for having the surface features appear as similar as possible in the sequential imagery, the imageries should be taken ideally at the same time of day.

Post-processing can also help in enhancing the quality of the output. After the estimation of the spatially varying misalignment of a pair of optical images by the offset tracking methods due to surface motion, the optical IV processing chain works as follows:

1. For each pixel, the maps are averaged in time weighted by the (inverse) root mean square (RMS) velocity difference of each pixel with respect to its 5x5 nearest neighbors. This means that regions where all pixels have similar flow are considered to be of good quality whereas regions where pixels appear to flow in different directions with different velocities are of bad quality (usually, a highly variable flow field indicates that we have attempted to derive IV of a cloud or a snow patch). Weighted temporal averaging removes these low-quality regions.
2. Individual 14-day blocks are merged into two kinds of season products:
    - One with all available 14-day blocks.
    - One with the temporal average over all 14-days blocks.

3. Finally, tiles are merged into glacier products.

4.6 Capabilities and known limitations

The applicability of offset tracking techniques is limited by the following factors:

- The temporal separation of the image acquisition pairs must be short enough for ice-sheet features to show little change in their appearance. This temporal separation is glacier and/or season dependent.
- Sun angle variations across the image. These variations reflect in solar illumination effects, which increase the noise in the imagery. A possibility for reducing this noise is to acquire imagery taken at the same time of day.

  Cloud coverage. The presence of clouds over ice and/or snow is one of the main sources of noise/failures for offset tracking-based algorithms. A possibility for reducing this noise is to apply clouds mask before performing offset tracking. Unfortunately, the cloud masks currently available do not present reliable output.
- The image pairs are already co-registered relative to basement features. This could be performed setting Ground Control Points or by using other methods.
- The presence of bed-related topographic features which remain stationary as the ice flows over them may distort the displacements measured.
- The motion of the for ice-sheet features should be translational only.

4.7 References

Bernstein, R. (1983), Image geometry and rectification, In Manual of Remote Sensing (R. N. Colwell, ed.), American Society of Photogrammetry, Falls Church, VA, pp.881-884

De Lange, R., A. Luckman, T. Murray Improvement of satellite radar feature tracking for ice velocity derivation by spatial frequency filtering, IEEE Trans. Geosc. Rem. Sens. 45, 2309-2317 (2007).

Derauw, D. DInSAR and Coherence Tracking Applied to Glaciology: The Example of Shirase Glacier, in proc. Fringe'96, (1996).

Gray, A.L., N. Short, K.E. Mattar and K.C. Jezek Velocities and flux of the Filchner ice shelf and its tributaries determined from speckle tracking interferometry, Canadian J. Rem. Sensing 27, 3 (2001).

Joughin, I. Ice-sheet velocity mapping: a combined interferometric and speckle-tracking approach, Annals of Glaciol. 34, 1, 195-201 (2002).

Lucchitta, B.K., C.E. Rosanova & K.F. Mullins Velocities of Pine Island glacier, West Antartica, from ERS-1 SAR images, Ann. Glaciol. 21, 277-283 (1995).

Michel, R. & E. Rignot Flow of Moreno glacier, Argentina, from repeat-pass Shuttle Imaging Radar images: comparison of the phase correlation method with radar interferometry, J. Glaciol. 45, 149, 93-100 (1999).

Scambos, T. A., Dutkiewicz, M. J., Wilson, J. C., and R. A. Bindschadler (1992): Application of image cross-correlation to the measurement of glacier velocity using satellite image data. Remote Sensing Environ., 42(3), 177-186.

Fahnestock, M. A., Scambos, T.A., and R. A. Bindschadler (1992): Semi-automated ice velocity determination from satellite imagery. Eos, 73, 493.

5 Gravimetric Mass Balance

5.1 Introduction

The Gravity Recovery and Climate Experiment (GRACE) (Tapley et al., 2004) satellite mission launched in 2002, and terminated its mission in October 2017. The GRACE mission has been highly successful in monitoring the mass loss of the Greenland ice sheet, and provided a clear and unambiguous time series of the mass loss through the GMB ECV (Gravimetric Mass Balance) for the Greenland ice sheet (including outlying glaciers and ice caps), highlighting the dynamic nature of the Greenland ice sheet changes, with record melt in 2012 followed by a decrease in yearly mass loss in the period 2013-17 (Shepherd et al., 2019).

The GRACE data used in the ESA Greenland CCI project, are based on monthly Level-2 gravity fields in spherical harmonics and are available in the period April 2002 through May 2017. As the GRACE mission aged, problems related to accelerometers and batteries in the spacecraft, as well as sunspot conditions, resulted in slightly increasing noise level in the Level 2 data from 2011 onwards. The accelerometer data in the GRACE-B spacecraft was finally turned off in October 2017, and GRACE-A accelerations "transplanted" to GRACE-B, resulting in significantly higher errors in GRACE Level-2 data at the end of the GRACE mission, and therefore also higher errors in the derived mass loss, especially at basin scales.

The GRACE-FO successor mission to GRACE employed a similar K/Ka band microwave tracking link as GRACE, with similar accelerometers to measure non-gravitational accelerations. The GRACE-FO mission (satellite pair GRACE-C and GRACE-D) was launched on May 22, 2018. Unfortunately, the GRACE-D accelerometer in GRACE-FO did not work properly, and GRACE-C data have been transplanted to GRACE-D, similar to the last period of GRACE. Level-2 data from GRACE-FO have been available since June 2018, leaving a 1-year gap in the GMB time series.

Advantages of the GRACE method are that it provides regional averages without the need for interpolation, measures the effect of mass fluctuations directly, and permits monthly temporal sampling. However, a key challenge is to discriminate fluctuations in ice-sheet mass from changes in the underlying crust and mantle. The spatial resolution of GRACE observations derived from global spherical harmonic solutions of about 300 km in the Polar Regions is coarse in comparison to that of other geodetic techniques. Hence, a further complicating factor is that signals may leak into regional GRACE solutions as a consequence of remote geophysical processes.

5.1 Scientific background update

Advantages of the GRACE monitoring of the ice sheets is that it provides regional averages without the need for interpolation, measures the effect of mass fluctuations directly, and permits monthly temporal sampling. However, a key challenge is to discriminate fluctuations in ice-sheet mass from changes in the underlying crust and mantle, especially due to GIA (Glacial Isostatic Adjustment). The disadvantage of GRACE observations is the limited resolution (~300 km) compared to satellite altimetry and ice velocity ECVs. A further complicating factor is that signals may leak into regional GRACE solutions; this is especially a problem in Greenland, where the melt signals of Canadian ice caps, especially in Ellesmere and Devon Islands, cannot be reliably separated from the Greenland melt, without use of auxiliary data, such altimetry-derived mass loss constraints.

For details of the background of the science see the ATBD of the Phase-2 of the CCI project, available at http://esa-icesheets-cci.org/index.php, under the link "Phase 2 documents", and the references in there. Some recent CCI-relevant GRACE papers include Bandikov et al (2019), Bettadpur et al (2018), Forsberg et al (2017), Groh et al (2019), and Shepherd et al (2019). Caron et al (2018) gives a review of GIA models including the recent model to be used in the CCI+ project.

The GRACE and GRACE-FO missions has two identical spacecraft flying about 220 km apart in a polar originally at 500 km above the Earth; the GRACE mission decayed to about 420 km during the mission period, so resolution actually increased during the mission time. The GRACE-FO has been launched to a similar polar orbit as GRACE, with a design lifetime of 5 years; its hoped that the lifetime will be much longer, as happened with GRACE.

GRACE- and GRACE-FO derived solutions of the Earth's time variable gravity field are available from different official processing facilities (CSR, GFZ and JPL). Level-2 products, provided as spherical harmonic coefficients (Stokes coefficients), are widely used in mass change studies. For the CCI project, independent solutions made at TU Graz was used in Phase-2 of the CCI project (2015-18); due to delays in generating new solutions, the release 6 (R6) of CSR (Center for Space Research, University of Austin) Level-2 products has been used for a parallel solution. The derived CCI products (time-averaged grids) and monthly estimates of the entire ice sheet, as well as 8 drainage basins (Figure 5.1).

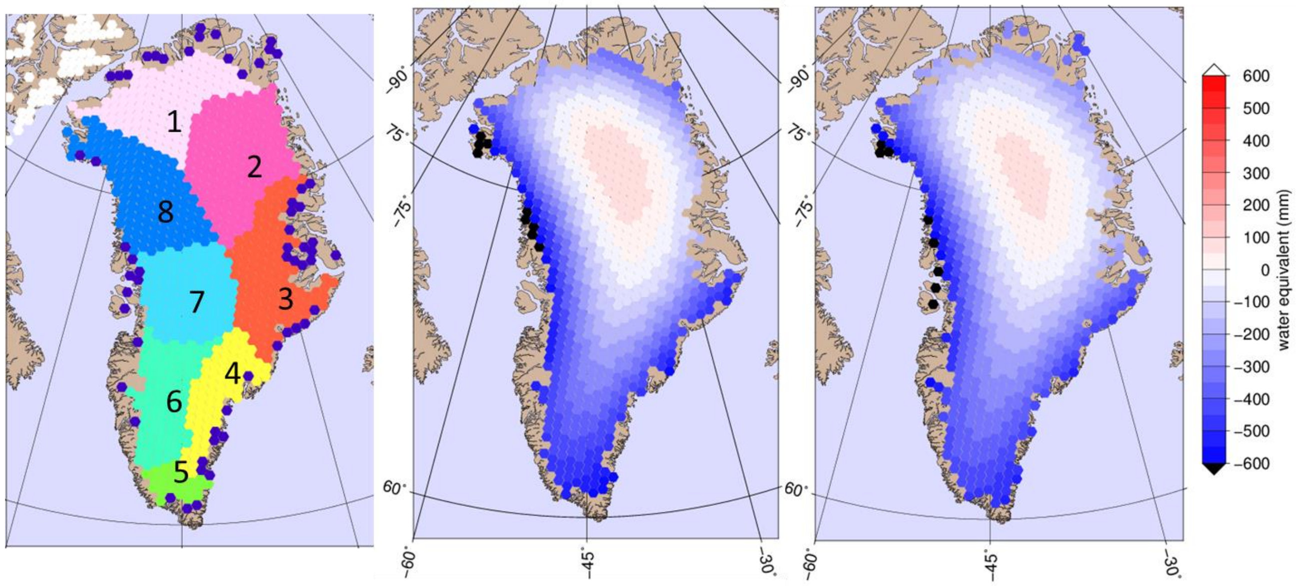

Figure 5.1: Overview of the drainage basin definition and the solution area (left). Blue dots to the left are cells for outlying glaciers and ice caps, some connected to the Greenland ice sheets, some un-connected. Map of trend without including the outer glaciers in the solution area (middle). Map of trend over the whole Greenland, that is including the outer glaciers (right). Due to the limited resolution of GRACE, large "leakage errors" prevent the separation of the ice sheet proper mass loss versus the outlying glaciers. The coast-near mass loss in NW Greenland are similarly impossible to separate from Ellesmere Island eastern ice cap mass losses.

While correlated errors are predominantly affecting the short wavelength (i.e. coefficients of higher spherical harmonic degrees), and shows up in "striping" errors, coefficients of low degrees are also subject to errors. To overcome this limitation C20 is replaced by an estimate derived from SLR observations. Degradation of C30 is mainly related to the use of transplanted accelerometer data. Hence, it is recommended to also replace it with SLR values for all months following August 2016 (Loomis et al., 2020). Gravity fields derived from GRACE data refer to the Earth's centre of mass (CM), where the degree-1 term is zero by definition. Therefore degree-1 (C10, C11, S11) estimates based on a combination of GRACE and geophysical model data are used to complement GRACE and the lowest degrees. The replacement values for the degree-1, C20 and C30 terms are given as independent files by the L2 processing centers (TN-13, TN-11, TN-14).

For GRACE-FO, exactly the same processing is applied as for the updated GRACE R6 data from CSR, using the same low-degree terms (recently updated for the whole mission). The data to be released will be based on the available CSR R6 data, and – when available – also the updated ITSG/TU Graz updated L2 data. For more details and references see the Phase 2 ATBD document.

The GRACE and GRACE-FO data shows apparently a good continuation and consistency between missions and is also consistent with long-term CryoSat-derived mass loss trends. Figure 5.2 shows an example of Greenland mass loss from GRACE and GRACE-FO data for the whole ice sheet, using the CCI mascon inversion scheme of DTU Space. An apparent good agreement in trend is seen, and data also highlights the anomalous melt in year 2019, consistent with a usually warm central W Greenland summer, matching the similar 2012 melt event.

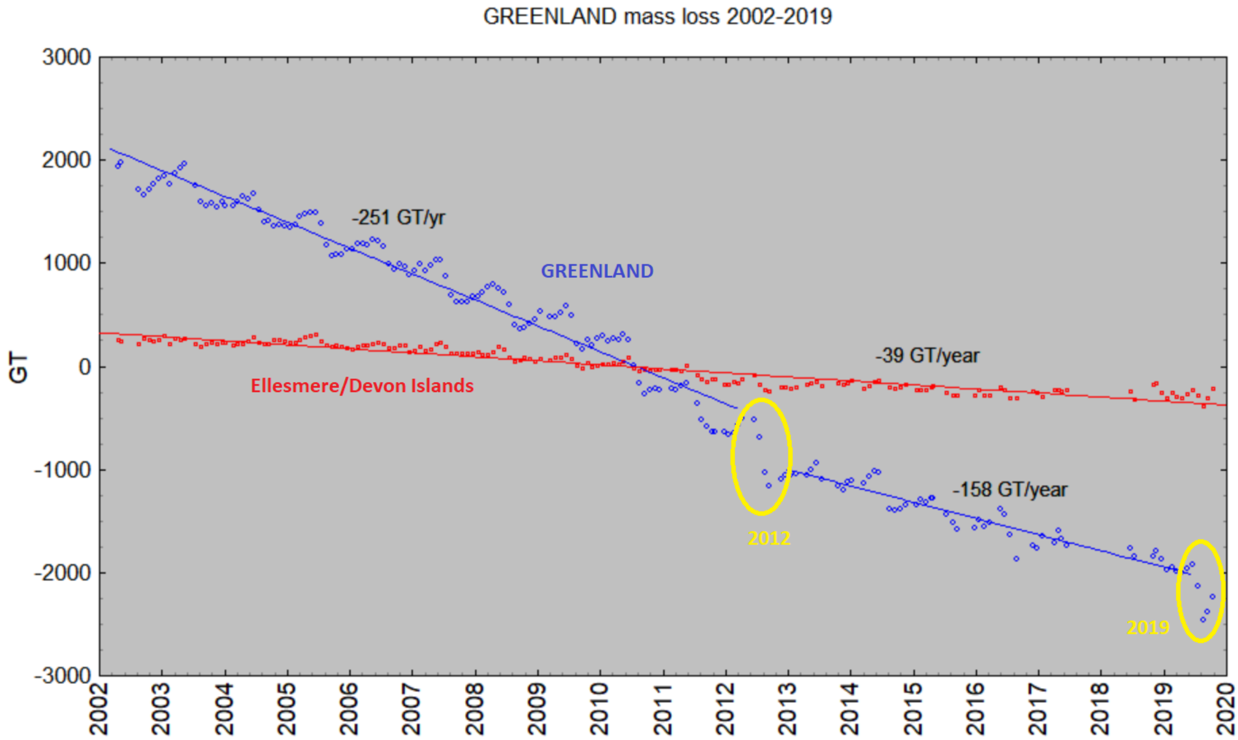

Figure 5.2: Mass loss of the Greenland ice sheet for the combined GRACE and GRCE-FO period (blue), shown along with the estimated mass loss of the Ellesmere Island and Devon Island, Canada, ice caps (red). The apparent continuity of GRACE and GRACE-FO is apparent. The 2012 and 2019 melt events in Greenland is also apparent. The apparent GRACE trends in 2002-2012 and 2013-2019 shows how the Greenland ice sheet melt surprisingly decelerated after the 2012 melt event.

5.2 Algorithms

Methods used for the inference of mass changes from GRACE data is divided into two main groups:

1. Inversion approaches (mascons), as implemented at DTU Space (Forsberg et al, 2018)

2. Regional integration approaches, as implemented at TU Dresden (Groh et al, 2019)

The mass inversion method has been adopted for the GMB product generation, primarily in order to be consistent with the ongoing GRACE result release at the national Danish Polarportal (www.polarportal.dk), but also because the mascon inversion approach make it more easy to separate overlapping signals ("leakage") from adjacent ice caps.

The regional integration approach used in the CCI mass change algorithms, is using tailored sensitivity kernels. These kernels are designed to minimize the sum of GRACE errors, derived from empirical error variance-covariance information, and signal leakage (Groh and Horwath, 2016). Details are outlined in the CCI Phase 2 documents.

The methods are applied for GRACE and GRACE-FO in completely the same way as outlined in the CCI Phase 2 ATBD, with the exception of the updated R6 Level 2 data, and the updated long-wavelength spherical harmonic terms for harmonic degrees 1,2 and 3, and the change of the GIA model.

5.3 Input data and algorithm output

Input for the GRACE mascon and regional integration approaches are the same: L2 data from CSR, and later expected L2 products from ITSG, TU Graz). The CSR and ITSG products are based on quite different constraints on the raw L1 GRACE/GRACE-FO data.

Because of the two methodologies used to produce the Greenland mass loss, and the two sets of R2 data, there will eventually be generated four time GRACE/GRACE-FO time series. The spread of these time series may be used as cross-validation and partially error estimates for the time series. From the Round-Robin exercise carried out in Phase 2 of the CCI project, and described in the Round-Robin report of the Phase-2 documents at http://esa-icesheets-cci.org. Typical errors estimated in this way are at the 10 GT/year magnitude.

5.4 Capabilities and known limitations

The GRACE time series are at the state-of-the art level, as a.o. confirmed in the recent IMBIE-2 exercise (Shepherd et al., 2019). The main limitations of all GRACE is in the resolution; the source of the mass changes regions of Greenland are known to be associated with a narrow coastal band, as well as with major outlet glacier and ice streams (as evident from the SEC results). Therefore combined approaches, merging multiple types of data (e.g. both SEC, IV/MFID and GMB) are needed to refine a more detailed GMB product; this is however an area of ongoing research, and the total or basin scale mass loss would likely not change much in such a combined product.

5.5 References

Bandikov T, C McCullough, G Kruizinga, H Save, B Christophe: GRACE accelerometer data transplant. Advances in Space Research, Volume 64, Issue 3, 1 August 2019, Pages 623-644, https://doi.org/10.1016/j.asr.2019.05.021

Barletta, V. R., Sørensen, L. S., and Forsberg, R. (2013). Scatter of mass changes estimates at basin scale for Greenland and Antarctica. The Cryosphere, 7(5), 1411–1432.

Bettadpur, S. (2018). UTCSR Level-2 Processing Standards Document for Level-2 Product Release 0006. Austin: Center for Space Research, The University of Texas at Austin.

Caron, L., Ivins, E. R., Larour, E., Adhikari, S., Nilsson, J., & Blewitt, G. (2018). GIA model statistics for GRACE hydrology, cryosphere, and ocean science. Geophysical Research Letters, 45, 2203–2212. https://doi.org/10.1002/2017GL076644

Groh, A., Horwath, M., Horvath, A., Meister, R., Sørensen, L. S., Barletta, V. R., Forsberg, R., Wouters, B., Ditmar, P., Ran, J., Klees, R., Su, X., Shang, K., Guo, J., Shum, C. K., Schrama, E., & Shepherd, A. (2019). Evaluating GRACE Mass Change Time Series for the Antarctic and Greenland Ice Sheet—Methods and Results. Geosciences, 9(10), 415.

Groh, A.; Horwath, M. The method of tailored sensitivity kernels for GRACE mass change estimates. In Proceedings of the EGU General Assembly 2016, Vienna, Austria, 17–22 April 2016; Volume 18.

Forsberg, R., Sørensen, L. & Simonsen, S: Greenland and Antarctica Ice Sheet Mass Changes and Effects on Global Sea Level. Surveys in Geophysics (2017) 38: 89. doi:10.1007/s10712-016-9398-7

Kvas, A., Behzadpour, S., Ellmer, M., Klinger, B., Strasser, S., Zehentner, N., & Mayer-Gürr, T. (2019). ITSG-Grace2018: Overview and Evaluation of a New GRACE-Only Gravity Field Time Series. J. Geophys. Res. Solid Earth, 124(8), 9332–9344.

Loomis, B. D., Rachlin, K. E., Wiese, D. N., Landerer, F. W., & Luthcke, S. B. (2020). Replacing GRACE/GRACE-FO C30 with satellite laser ranging: Impacts on Antarctic Ice Sheet mass change. *Geophys. Res. Lett.*, . doi:10.1029/2019GL085488.

Shepherd, A, E Ivins, E Rignot, B Smith, M van den Broeke, I Velicogna, P Whitehouse, K Briggs, I Joughin, G Krinner, S Nowicki, T Payne, T Scambos, N Schlegel, A Geruo, C Agosta, A Ahlstrøm, G Babonis, V Barletta, A Bjørk, A Blazquez, J Bonin, W Colgan, B Csatho, R Cullather, M Engdahl, D Felikson, X Fettweis, R Forsberg, A Hogg, H Gallee, A Gardner, L Gilbert, N Gourmelen, A Groh, B Gunter, E Hanna, C Harig, V

Helm, A Horvath, M Horwath, A Khan, K Kjeldsen, H Konrad, P Langen, B Lecavalier, B Loomis, S Luthcke, M McMillan, D Melini, S Mernild, Y Mohajerani, P Moore, R Mottram, J Mouginot, G Moyano, A Muir, T Nagler, G Nield, J Nilsson, B Noël, I Otosaka, M Pattle, R Peltier, N Pie, R Rietbroek, H Rott, L Sørensen, I Sasgen, H Save, B Scheuchl, E Schrama, L Schröder, K Seo, S Simonsen, T Slater, G Spada, T Sutterley, M Talpe, L Tarasov, W van de Berg, W van der Wal, M Wessem, B Vishwakarma, D Wiese, D Wilton, T Wagner, B Wouters, J Wuite: Mass balance of the Greenland Ice Sheet from 1992 to 2018. Nature (2019) doi:10.1038/s41586-019-1855-2

6 Mass Flow Rate and Ice Discharge

Here we present the mass flow rate and ice discharge (MFID). This work is based on the published data, algorithm, and code from Mankoff et al. (2019) but with the following changes:

- We only use CCI Ice Velocity (IV) data.
- The baseline velocity, used to place the discharge gates, is the average 2018 velocity.
- Surface elevation change (from Simonsen and Sørensen (2017), Sørensen et al. (2015), Khvorostovsky (2012), and S. Sørensen et al. (2015)) is only applied in a few cases where the two data overlap.
- Gates are 10 km upstream from the baseline termini, rather than 5 km as in Mankoff et al. (2019).
- Cutoff velocity is 150 m yr-1 rather than 100 m yr-1 as Mankoff et al. (2019).

Note that much of the text below is from Mankoff et al. (2019) and is reproduced here either verbatim, or with minor changes to reflect minor changes in the work presented here.

6.1 Introduction

The mass of the Greenland ice sheet is decreasing (e.g. Fettweis et al. (2017), van den Broeke et al. (2017), Wiese et al. (2016), and Khan et al. (2016)). Most ice sheet mass loss – as iceberg discharge, submarine melting, and meltwater runoff – enters the fjords and coastal seas, and therefore ice sheet mass loss directly contributes to sea-level rise (WCRP Global Sea Level Budget Group 2018; Moon et al. 2018; Nerem et al. 2018; Chen et al. 2017). Greenland's total ice loss can be estimated through a variety of independent methods, for example 'direct' mass change estimates from GRACE (Wiese et al. 2016) or by using satellite altimetry to estimate surface elevation change, which is then converted into mass change (using a firn model, e.g. Khan et al. (2016)). However, partitioning the mass loss between ice discharge (D) and surface mass balance (SMB) remains challenging (c.f. Rignot et al. (2008) and Enderlin et al. (2014)). Correctly assessing mass loss, as well as the attribution of this loss (SMB or D) is critical to understanding the process-level response of the Greenland ice sheet to climate change, and thus improving models of future ice-sheet changes and associated sea-level rise (Moon et al. 2018).

6.2 Review of scientific background

The total mass of an ice-sheet, or a drainage basin, changes if the mass gain (SMB inputs, primarily snowfall) is not balanced by the mass loss (D and SMB outputs, the latter generally meltwater runoff). This change is typically termed ice-sheet mass balance (MB) and the formal expression for this rate of change in mass is (e.g. Cuffey and Paterson (2010)),

$$\frac{\mathrm{d}M}{\mathrm{d}t} = \rho \int_A b \ \mathrm{d}A - \int_g Q \ \mathrm{d}g, \qquad \textbf{(Equation 6.1)}$$

where ρ is the average density of ice, b is an area mass balance, and Q is the discharge flux. The left hand side of the equation is the rate of change of mass, the first term on the right hand side is the area A integrated surface mass balance (SMB), and the second term is the discharge D mass flow rate that drains through gate g. The Equation above is often simplified to

$$\boldsymbol{MB = SMB - D} \qquad \textbf{(Equation 6.2)}$$

where MB is the mass balance, and referred to as the "input-output" method (e.g. Khan et al. (2015)). Virtually all studies agree on the trend of Greenland mass balance, but large discrepancies persist in both the magnitude and attribution. Magnitude discrepancies include, for example, Kjeldsen et al. (2015) reporting a mass imbalance of -250 $\pm$ 21 Gt yr-1 during 2003 to 2010, Ewert, Groh, and Dietrich (2012) reporting -181 $\pm$ 28 Gt yr-1 during 2003 to 2008, and Rignot et al. (2008) reporting a mass imbalance of -265 $\pm$ 19 Gt yr-1 during 2004 to 2008. Some of these differences may be due to different ice sheet area masks used in the studies. Attribution discrepancies include, for example, Enderlin et al. (2014) attributing the majority (64 %) of mass loss to changes in SMB during the 2005 to 2009 period but Rignot et al. (2008) attributing the majority (85 %) of mass loss to changes in D during the 2004 to 2008 period.

Discharge may be calculated through several methods, including mass flow rate through gates (e.g. Enderlin et al. (2014), King et al. (2018), and J. Mouginot et al. (2019)), or solving as a residual from independent mass balance terms (e.g. Kjær et al. (2012; Kjeldsen et al. 2015)). The gate method that we use in this study incorporates ice thickness and an estimated vertical profile from the observed surface velocity to calculate the discharge. A typical formulation of discharge across a gate D_g is,

$$\boldsymbol{D_g = \rho V H w},\qquad \textbf{(Equation 6.3)}$$

where ρ is the average density of ice, V is depth-average gate-perpendicular velocity, H is the ice thickness, and w is the gate width. Uncertainties in V and H naturally influence the estimated discharge. At fast-flowing outlet glaciers, V is typically assumed to be equal at all ice depths, and observed surface velocities can be directly translated into depth-averaged velocities (as in Enderlin et al. (2014), and King et al. (2018)). To minimize uncertainty from SMB or basal mass balance corrections downstream of a flux gate, the gate should be at the grounding line of the outlet glacier. Unfortunately, uncertainty in bed elevation (translating to ice thickness uncertainty) increases toward the grounding line. To minimize downstream SMB effects, we put gates as close as possible to the grounding line.

6.3 Algorithms

6.3.1 Terminology

We use the following terminology:

- "Pixels" are individual 200 m x 200 m raster discharge grid cells. We use the nearest neighbor when combining data sets that have different grid properties.
- "Gates" are contiguous (including diagonal) clusters of pixels.
- "Sectors" are spatial areas that have 0, 1, or > 1 gate(s) plus any upstream source of ice that flows through the gate(s), and come from Zwally et al. (2012).
- The "baseline" period is the average 2018 velocity from all available 2018 CCI IV data.
- "Fast-flowing ice" is defined as ice that flows more than 150 m yr^{-1}.
- Names are reported using the official Greenlandic names from Bjørk, Kruse, and Michaelsen (2015) if a nearby name exists, then Mouginot and Rignot (2019) in parentheses.

Although we refer to solid ice discharge, and it is in the solid phase when it passes the gates and eventually reaches the termini, submarine melting does occur at the termini and some of the discharge enters the fjord as liquid water (Enderlin and Howat 2013).

6.3.2 Gate location

Gates are algorithmically generated for fast-flowing ice (greater than 150 m yr^{-1}) close to the ice sheet terminus determined by the baseline-period data. We apply a 2D inclusive mask to the baseline data for all ice flowing faster than 150 m yr^{-1}. We then select the mask edge where it is near the BedMachine ice mask (not including ice shelves), which effectively provides grounding line termini. We buffer the termini 10 km in all directions creating ovals around the termini and once again down-select to fast-flowing ice pixels. This procedure results in gates 10 km upstream from the baseline terminus that bisect the baseline fast-flowing ice. We manually mask some land- or lake-terminating glaciers which are initially selected by the algorithm due to fast flow and mask issues.

We select a 150 m yr^{-1} speed cutoff because slower ice, taking longer to reach the terminus, is more influenced by SMB. The choice of a 10 km buffer follows from the fact that it is near-terminus and thus avoids the need for (minor) SMB corrections downstream, yet is not too close to the terminus where discharge results are sensitive to the choice of distance-to-terminus value (Mankoff et al. 2019), which may be indicative of bed (ice thickness) errors.

6.3.3 Thickness

We derive thickness from the BedMachine surface and bed elevation. We adjust the surface through time by linearly interpolating the SEC product and adding it to the BedMachine surface, where the SEC product exists. Finally, from the fixed bed and temporally varying surface, we calculate the time-dependent ice thickness at each gate pixel.

6.3.4 Missing or invalid data

The baseline data provides velocity at all gate locations by definition, but individual non-baseline velocity maps often have missing or invalid data. Also, thickness provided by BedMachine is clearly incorrect in some places (e.g. fast-flowing ice that is 10 m thick, Figure 6.1). We define invalid data and fill in missing data as described below.

1. Missing IV

   We generate an ice speed time series by assigning the IV product to the middle of their reported time span. Velocities are sampled only where there are gate pixels. Missing pixel velocities are linearly interpolated in time, except for missing data at the beginning of the time series which are back- and forward-filled with the temporally-nearest value for that pixel.

2. Missing SEC

   Where SEC is missing, we use the provided BedMachine ice thickness.

3. Invalid thickness

   The thickness data appear to be incorrect in some locations. For example, many locations have fast-flowing ice, but report ice thickness as 10 m or less. We accept all ice thickness greater than 20 m and construct from this a thickness versus $\log_{10}$ speed relationship. For all ice thickness less than or equal to 20 m thick we adjust thickness based this relationship. We selected the 20 m thickness cutoff after visually inspecting the velocity distribution. This thickness adjustment adds 20 Gt yr^{-1} to our baseline-period discharge estimate with no adjustment.

6.3.5 Discharge

We calculate discharge per pixel using density (917 kg m^{-3}), Filled ice velocity, projection-corrected pixel width, and adjusted ice thickness derived from time-varying surface elevation and a fixed bed elevation. We assume that any change in surface elevation corresponds to a change in ice thickness and thereby neglect basal uplift, erosion, and melt, which combined are orders of magnitude less than surface melting (e.g. Cowton et al. (2012), Khan et al. (2007)). We also assume depth-averaged ice velocity is equal to the surface velocity.

We calculate discharge using the gate-orthogonal velocity at each pixel and at each timestamp – all velocity estimates are gate-orthogonal at all times, regardless of gate position, orientation, or changing glacier velocity direction over time.

6.4 Input data and algorithm output

6.4.1 Input Data

The discharge gates in this study are generated using only surface speed and an ice mask. We use CCI ice velocity (IV) and the BedMachine v3 (M. Morlighem, Williams, et al. 2017a, 2017b) ice mask, and BedMachine for initial ice thickness, supplemented with the SEC product from this project. Official glacier names come from Bjørk, Kruse, and Michaelsen (2015). Other glacier names come from Mouginot and Rignot (2019).

Table 6.1: Summary of data sources used in this work.

Property	Name used in this paper	Reference
Basal Topography	BedMachine	M. Morlighem, Williams, et al. (2017a, 2017b)
Surface Elevation	BedMachine	M. Morlighem, Williams, et al. (2017a, 2017b)
Surface Elevation Change	Surface Elevation Change	CCI+ SEC
Baseline Velocity	Baseline	CCI+ IV 2-18 average
Velocity	CCI IV	CCI+ IV
Sectors & Regions	Sectors & Regions	Mouginot and Rignot (2019)
Names		Bjørk, Kruse, and Michaelsen (2015; Mouginot and Rignot 2019)

6.4.2 Algorithm Output

The output of the algorithm is a set of CSV files with time (quarterly) and discharge (by region from Zwally et al. (2012)). Table shows the algorithm output.

6.5 Accuracy and performance

6.5.1 Accuracy

The algorithm and data product introduced here are closely related to the algorithm and data product introduced by Mankoff et al. (2019). When comparing annual average over all of Greenland, then this product and the product released by Mankoff et al. (2019) agree well. Comparing by regions is difficult because this product is binned on the Zwally et al. (2012) and Mankoff et al. (2019) is on the Mouginot and Rignot (2019) regions and sectors.

Table 6.2: Comparison between this product ("this") and Mankoff et al. (2019) ("m2019")

Date	this	$this_{err}$	m2019	$m2019_{err}$	Diff	diff %
2014-10-31	458.201	41.714	493.947	50.835	-35.746	-7.80
2014-11-30	458.064	41.684	499.001	51.361	-40.937	-8.93
2014-12-31	458.933	41.739	499.686	51.421	-40.753	-8.87
2015-01-31	459.531	41.785	498.548	51.119	-39.016	-8.49
2015-02-28	458.165	41.595	498.392	50.959	-40.226	-8.77
2015-03-31	464.214	42.119	500.767	51.545	-36.553	-7.87
2015-04-30	471.51	42.758	0	0	471.51	100
2015-05-31	481.213	43.613	498.79	51.057	-17.577	-3.65
2015-06-30	484.541	43.863	0	0	484.541	100
2015-07-31	476.351	42.776	515.999	52.900	-39.648	-8.32
2015-08-31	466.619	42.14	498.024	50.989	-31.405	-6.73
2015-09-30	463.94	41.987	500.495	51.367	-36.555	-7.87
2015-10-31	460.43	41.725	498.883	51.175	-38.453	-8.35
2015-11-30	464.914	42.103	0	0	464.914	100
2015-12-31	459.72	41.69	499.037	51.197	-39.317	-8.55
2016-01-31	458.423	41.547	493.502	50.658	-35.07	-7.65
2016-02-29	457.078	41.436	0	0	457.07	100

2016-03-31	456.667	41.487	492.947	50.691	-36.28	-7.94
2016-04-30	470.318	42.652	0	0	470.31	100
2016-05-31	476.316	43.147	498.546	51.527	-22.23	-4.66
2016-06-30	482.292	43.864	0	0	482.29	100
2016-07-31	484.153	43.746	504.007	51.724	-19.854	-4.10
2016-08-31	468.55	42.54	493.635	50.693	-25.085	-5.35
2016-09-30	463.512	42.22	495.268	50.779	-31.756	-6.85
2016-10-31	476.721	43.55	495.857	50.883	-19.136	-4.01
2016-11-30	477.397	43.765	497.649	50.985	-20.251	-4.24
2016-12-31	477.492	43.789	497.671	50.958	-20.178	-4.22
2017-01-31	467.408	43.152	500.478	51.104	-33.069	-7.07
2017-02-28	469.127	43.734	500.683	51.156	-31.555	-6.72
2017-03-31	475.137	44.192	500.946	51.152	-25.809	-5.43
2017-04-30	480.697	44.753	507.796	52.366	-27.099	-5.63
2017-05-31	497.159	46.091	508.157	52.198	-10.997	-2.21
2017-06-30	499.296	46.247	507.599	51.486	-8.303	-1.66
2017-07-31	511.125	47.02	516.857	52.238	-5.732	-1.12
2017-08-31	495.171	45.175	507.64	51.063	-12.468	-2.51
2017-09-30	485.009	44.618	503.394	50.932	-18.385	-3.79
2017-10-31	486.657	44.754	506.185	51.447	-19.527	-4.01
2017-11-30	486.16	44.813	500.558	50.628	-14.398	-2.96
2017-12-31	483.653	44.649	501.124	50.796	-17.470	-3.61
2018-01-31	475.525	43.983	501.139	51.101	-25.614	-5.38
2018-02-28	475.491	43.971	499.779	50.901	-24.287	-5.10
2018-03-31	479.596	44.512	497.692	50.549	-18.096	-3.77
2018-04-30	481.411	44.726	495.004	50.165	-13.592	-2.82
2018-05-31	490.03	45.563	501.054	51.082	-11.024	-2.24
2018-06-30	498.167	46.298	496.822	50.772	1.345	0.26
2018-07-31	501.924	46.577	500.902	50.922	1.021	0.20
2018-08-31	491.054	44.961	497.571	50.385	-6.517	-1.32
2018-09-30	480.914	44.18	487.941	49.487	-7.027	-1.46
2018-10-31	480.203	44.399	499.935	51.104	-19.732	-4.10
2018-11-30	482.441	44.774	498.129	50.659	-15.688	-3.25
2018-12-31	478.485	44.463	496.089	50.685	-17.604	-3.67
2019-01-31	477.047	44.43	498.34	51.198	-21.293	-4.46
2019-02-28	481.548	44.936	497.903	51.034	-16.354	-3.39
2019-03-31	482.447	45.126	495.642	50.532	-13.195	-2.73
2019-04-30	491.115	45.852	499.428	51.132	-8.313	-1.69
2019-05-31	497.503	46.409	502.146	51.749	-4.643	-0.93
2019-06-30	513.127	48.037	507.756	52.096	5.370	1.04
2019-07-31	505.819	46.779	505.35	51.441	0.469	0.09

Comparing by regions is difficult because this product is binned on the Zwally et al. (2012) and Mankoff et al. (2019) is on the Mouginot and Rignot (2019) regions and sectors.

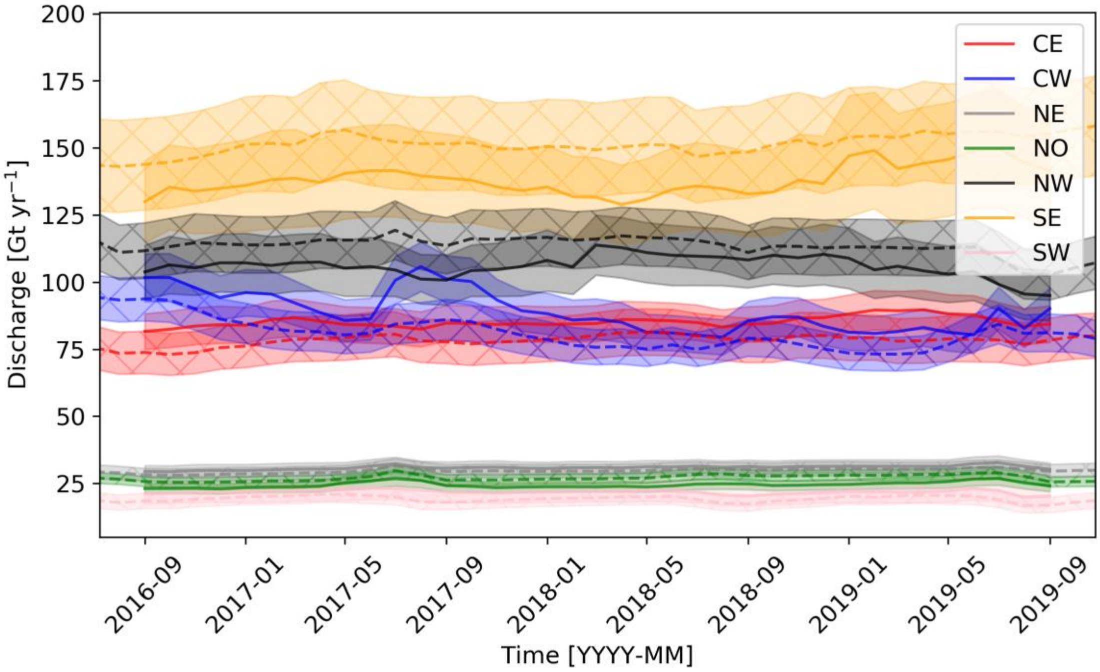

Figure 6.1: Comparison between this and Mankoff et al. (2019) monthly discharge by region. Solid line is this product, and solid fill is this product uncertainty. Dashed line and hatch fill are Mankoff et al. (2019).

6.5.2 Performance

The code takes ~1 hour to run after the input data products have been downloaded and placed in the necessary location. Downloading input data and installing all required software is not automated, but once those dependencies are met, the algorithm is publicly available.

Repeated runs make some use of the static computational results of earlier runs, and take less time to calculate discharge for updated velocity products.

If surface elevation change or thickness products change, a full re-run is required.

6.6 Capabilities and known limitations

We note the following major limitations to the current implementation.

- Discharge is only calculated where gates are placed. This means discharge less than the cutoff velocity is not considered, and that if a glacier does not currently have a gate surges in the future, that surge will not be captured in the discharge unless the gates are recalculated.
- We use relatively raw products as-provided from 3rd parties. We do not apply smoothing filters to the velocity product, and only adjust the thickness product where it is clearly incorrect (fast-flowing ice < 20 m thick).

There is only partial treatment of surface elevation change, because the CCI SEC product does not provide data near the coast.

6.7 References

Bjørk, A. A., L. M. Kruse, and P. B. Michaelsen. 2015. "Brief Communication: Getting Greenland's Glaciers Right – a New Dataset of All Official Greenlandic Glacier Names." *The Cryosphere* 9 (6): 2215–8. https://doi.org/10.5194/tc-9-2215-2015.

Chen, Xianyao, Xuebin Zhang, John A. Church, Christopher S. Watson, Matt A. King, Didier Monselesan, Benoit Legresy, and Christopher Harig. 2017. "The Increasing Rate of Global Mean Sea-Level Rise During 1993–2014." *Nature Climate Change* 7 (7): 492–95. https://doi.org/10.1038/nclimate3325.

Cowton, T., Peter Nienow, Ian D. Bartholomew, A. Sole, and Douglas W. F. Mair. 2012. "Rapid Erosion Beneath the Greenland Ice Sheet." *Geology* 40: 343–46. https://doi.org/10.1130/G32687.1.

Cuffey, Kurt M., and W. S. B. Paterson. 2010. *The Physics of Glaciers*. Fourth. Academic Press.

Enderlin, Ellyn M., and Ian M. Howat. 2013. "Submarine Melt Rate Estimates for Floating Termini of Greenland Outlet Glaciers (2000 – 2010)." *Journal of Glaciology* 59 (213): 67–75. https://doi.org/10.3189/2013JoG12J049.

Enderlin, Ellyn M., Ian M. Howat, Seongsu Jeong, Myoung-Jong Noh, Jan H. van Angelen, and Michiel R. van den Broeke. 2014. "An Improved Mass Budget for the Greenland Ice Sheet." *Geophysical Research Letters* 41 (3): 866–72. https://doi.org/10.1002/2013GL059010.

Ewert, H., A. Groh, and R. Dietrich. 2012. "Volume and Mass Changes of the Greenland Ice Sheet Inferred from ICESat and GRACE." *Journal of Geodynamics* 59-60 (September): 111–23. https://doi.org/10.1016/j.jog.2011.06.003.

Fettweis, Xavier, Jason E. Box, Cécile Agosta, Charles Amory, Christoph Kittel, Charlotte Lang, Dirk Van As, Horst Machguth, and Hubert Gallée. 2017. "Reconstructions of the 1900–2015 Greenland Ice Sheet Surface Mass Balance Using the Regional Climate MAR Model." *The Cryosphere* 11 (2): 1015–33. https://doi.org/10.5194/tc-11-1015-2017.

Khan, S. A., I. Sasgen, M. Bevis, T. van Dam, J. L. Bamber, J. Wahr, M. Willis, et al. 2016. "Geodetic Measurements Reveal Similarities Between Post-Last Glacial Maximum and Present-Day Mass Loss from the Greenland Ice Sheet." *Science Advances* 2 (9): e1600931–e1600931. https://doi.org/10.1126/sciadv.1600931.

Khan, Shfaqat A, Andy Aschwanden, Anders A Bjørk, John Wahr, Kristian K Kjeldsen, and Kurt H Kjær. 2015. "Greenland Ice Sheet Mass Balance: A Review." *Reports on Progress in Physics* 78 (4): 046801. https://doi.org/10.1088/0034-4885/78/4/046801.

Khan, Shfaqat A., John Wahr, Leigh A. Stearns, Gordon S. Hamilton, Tonie van Dam, Kristine M. Larson, and Olivier Francis. 2007. "Elastic Uplift in Southeast Greenland Due to Rapid Ice Mass Loss." *Geophysical Research Letters* 34 (21). https://doi.org/10.1029/2007gl031468.

Khvorostovsky, Kirill S. 2012. "Merging and Analysis of Elevation Time Series over Greenland Ice Sheet from Satellite Radar Altimetry." *IEEE Transactions on Geoscience and Remote Sensing* 50 (1): 23–36. https://doi.org/10.1109/tgrs.2011.2160071.

King, Michalea D., Ian M. Howat, Seongsu Jeong, Myoung J. Noh, Bert Wouters, Brice Noël, and Michiel R. van den Broeke. 2018. "Seasonal to Decadal Variability in Ice Discharge from the Greenland Ice Sheet." *The Cryosphere* 12 (12): 3813–25. https://doi.org/10.5194/tc-12-3813-2018.

Kjeldsen, Kristian K., Niels J. Korsgaard, Anders A. Bjørk, Shfaqat A. Khan, Jason E. Box, Svend Funder, Nicolaj K. Larsen, et al. 2015. "Spatial and Temporal Distribution of Mass Loss from the Greenland Ice Sheet Since AD 1900." *Nature* 528 (7582): 396–400. https://doi.org/10.1038/nature16183.

Kjær, Kurt H., Shfaqat A. Khan, Niels J. Korsgaard, John Wahr, Jonathan L. Bamber, Ruud Hurkmans, Michiel R. Van Den Broeke, et al. 2012. "Aerial Photographs Reveal Late-20th-Century Dynamic Ice Loss in Northwestern Greenland." *Science* 337 (6094): 569–73. https://doi.org/10.1126/science.1220614.

Mankoff, Kenneth D., William Colgan, Anne Solgaard, Nanna B. Karlsson, Andreas P. Ahlstrøm, Dirk van As, Jason E. Box, et al. 2019. "Greenland Ice Sheet Solid Ice Discharge from 1986 Through 2017." *Earth System Science Data* 11 (2): 769–86. https://doi.org/10.5194/essd-11-769-2019.

Moon, Twila, Andreas Ahlstrøm, Heiko Goelzer, William Lipscomb, and Sophie Nowicki. 2018. "Rising Oceans Guaranteed: Arctic Land Ice Loss and Sea Level Rise." *Current Climate Change Reports*, July. https://doi.org/10.1007/s40641-018-0107-0.

Morlighem, M., C. N. Williams, E. Rignot, L. An, J. E. Arndt, J. L. Bamber, G. Catania, et al. 2017a. "BedMachine V3: Complete Bed Topography and Ocean Bathymetry Mapping of Greenland from Multi-Beam Echo Sounding Combined with Mass Conservation." *Geophysical Research Letters*, September. https://doi.org/10.1002/2017gl074954.

Morlighem, M., C. Williams, E. Rignot, L. An, J. E. Arndt, J. Bamber, G. Catania, et al. 2017b. "IceBridge BedMachine Greenland, Version 3." NASA National Snow; Ice Data Center Distributed Active Archive Center. Boulder, Colorado USA: NASA National Snow; Ice Data Center Distributed Active Archive Center. https://doi.org/10.5067/2CIX82HUV88Y.

Mouginot, Jeremie, and Eric Rignot. 2019. "Glacier Catchments/Basins for the Greenland Ice Sheet." UC Irvine. https://doi.org/10.7280/d1wt11.

Mouginot, Jérémie, Eric Rignot, Anders A. Bjørk, Michiel van den Broeke, Romain Millan, Mathieu Morlighem, Brice Noël, Bernd Scheuchl, and Michael Wood. 2019. "Forty-Six Years of Greenland Ice Sheet Mass Balance from 1972 to 2018." *Proceedings of the National Academy of Sciences*, April, 201904242. https://doi.org/10.1073/pnas.1904242116.

Nerem, R. S., B. D. Beckley, J. T. Fasullo, B. D. Hamlington, D. Masters, and G. T. Mitchum. 2018. "Climate-Change–Driven Accelerated Sea-Level Rise Detected in the Altimeter Era." *Proceedings of the National Academy of Sciences* 115 (9): 2022–5. https://doi.org/10.1073/pnas.1717312115.

Rignot, Eric J., Jason E. Box, Evan W. Burgess, and Edward Hanna. 2008. "Mass Balance of the Greenland Ice Sheet from 1958 to 2007." *Geophysical Research Letters* 35 (L20502). https://doi.org/10.1029/2008GL035417.

Simonsen, Sebastian B., and Louise Sandberg Sørensen. 2017. "Implications of Changing Scattering Properties on Greenland Ice Sheet Volume Change from Cryosat-2 Altimetry." *Remote Sensing of Environment* 190 (March): 207–16. https://doi.org/10.1016/j.rse.2016.12.012.

Sørensen, Louise Sandberg, Sebastian B. Simonsen, Rakia Meister, René Forsberg, Joanna F. Levinsen, and Thomas Flament. 2015. "Envisat-Derived Elevation Changes of the Greenland Ice Sheet, and a Comparison with ICESat Results in the Accumulation Area." *Remote Sensing of Environment* 160 (April): 56–62. https://doi.org/10.1016/j.rse.2014.12.022.

Sørensen, S., S. Simonsen, R. Meister, R. Forsberg, and K. Khvorostovsky. 2015. "Surface Elevation Changes of the Greenland Ice Sheet from Satellite Radar Altimetry."

van den Broeke, Michiel, Jason Box, Xavier Fettweis, Edward Hanna, Brice Noël, Marco Tedesco, Dirk Van As, Willem Jan Van De Berg, and Leo Van Kampenhout. 2017. "Greenland Ice Sheet Surface Mass Loss: Recent Developments in Observation and Modeling." *Current Climate Change Reports*, November. https://doi.org/10.1007/s40641-017-0084-8.
WCRP Global Sea Level Budget Group. 2018. "Global Sea-Level Budget 1993 *Present*." *Earth System Science Data* 10 (3): 1551–90. https://doi.org/10.5194/essd-10-1551-2018.

Wiese, D. N., D.-N. Yuan, C. Boening, F. W. Landerer, and M. M. Watkins. 2016. "JPL GRACE Mascon Ocean, Ice, and Hydrology Equivalent HDR Water Height RL05M.1 CRI Filtered Version 2." PO.DAAC, CA, USA. https://doi.org/10.5067/TEMSC-2LCR5.

Zwally, H. Jay, M. Giovinetto, M. A. Beckley, and Jack L. Saba. 2012. "Antarctic and Greenland Drainage Systems." http://icesat4.gsfc.nasa.gov/cryo_data/ant_grn_drainage_systems.php.

7 Supraglacial Lake

7.1 Introduction

This section gives an overview of the identification of supra glacial (SL) lakes on the Greenland Ice sheet using dual threshold NDWI applied to sentinel-2 imagery.

7.2 Review of scientific background

The mapping of water bodies is based generally on a set of standard indices that enhance the spectral signature of water, the most readily used being the NDWI index. The spectral signature of water changes based on factors such as sediment loading or algae, water depth, and atmospheric conditions at the time of data acquisition (Feng et al., 2015; Pekel et al., 2016). Because of this, index thresholds vary in time and space, and may be scene dependent in some cases (Feng et al., 2015). This method is based on and adapted Yang and Smith (2013) method.

7.3 Algorithms

The main aim of this algorithm development is to develop a simple, robust method for distinguishing water bodies across most scenes. Sentinel-2 (S2) has been chosen as the data source for the optical algorithm development due to its high spatial, spectral and temporal resolution. Additionally, there is high availability of S2 imagery (with both S2A and S2B) through online APIs such as Sentinel Hub and Copernicus, thus increasing the chances for cloud-free scene acquisition.

The data downloaded from the ESA server are the level L1C data, giving per-pixel radiometric measurements of Top Of Atmosphere (TOA) reflectance. TOA data has been selected because full atmospheric correction of data over Greenland is not trivial and can easily introduce more errors.

Terrain shadow is a major source of error in water body classification, with many implementing terrain shadow masking and slope thresholds to limit false classifications (Feyisa et al., 2014; Feng et al., 2015). Here, the risk of false classification from terrain shadow is minimal as the Greenland Ice Sheet is largely flat. Therefore, terrain shadow correction has not been included in this algorithm development for SL delineation.

The spectral indices given in Table 7.1 were used within a series of threshold filtering steps to classify water bodies.

Table 7.1: Multi-spectral indices used for water body classification, including the S2 spectral bands used. For more information on S2 spectral band wavelengths, see https://earth.esa.int/web/sentinel/user-guides/sentinel-2-msi/resolutions/radiometric

Index	Bands used	Expression	Target	Reference
NDWI	S2 green band (B3) S2 near-infrared band (B8)	$(B3 - B8)/(B3 + B8)$	Water + shadows = high Sediment-loaded water + snow/ice = medium Other land classes = low	McFeeters (1996)

Scene selection is limited to the drainage catchment, and within the melt season when the water bodies are less likely to be ice-covered. The spectral indices are calculated for each scene, as described in Table 7.1.

All processing was carried out using Python (v3), namely the ArcPy package within ArcGIS Pro. Key dependencies for running the script are:

- Arcpy (v1.2.5), for performing geographic data analysis, data conversion, and data management
- Geopandas (v0.4.1), for data handling
- Glob (v0.6), for handling file directories and pathnames

The processing chain operate as standalone scripts.

The SL detection method largely utilises the ArcGIS python package ArcPy for handling and manipulating raster data; for instance, using the 'ExtractByMask' algorithm for raster masking, and the 'Reclassify' algorithm for generating binary matrices from NDWI images.

The workflow of the method can be simplified to five key steps:

1. Create the NDWI raster files
2. Create the binary rasters, based on upper and lower threshold limits (dual threshold)
3. Mask the binary rasters, using a shapefile denoting the ice catchment (if provided)
4. Vectorise the binary rasters, only retaining positive matches
5. Filter vectorised polygons to remove false matches in a two-step process:
    a. SLs below a given area threshold (<0.01 sq km) are removed as they are deemed as misclassification, e.g. water filled crevasses and saturated snow.
    b. SLs within a mask denoting sinks in the ice surface are retained (if provided), and those outside the mask are filtered by a second threshold of <0.02 sq km
6. Merge overlapping polygons derived from upper and lower threshold limits, grouping common lakes between time steps
7. Assign information to each SL detected (i.e. area, perimeter, time slice, satellite tile detected from), and combine them from each time slice into individual outputted shapefiles for each unique acquisition

Additionally, two masks are used to streamline the detection algorithm and filter results. The first (used in step 3) is a hydrological catchment mask used to limit SL classification to the area of interest, which was sourced from the PROMICE database (Mankoff et al.). The second mask (used in step 5b) is a sink mask generated from flow routing analysis of the ice surface (using ArcticDEM), producing potential a filled sink mask for meltwater accumulation. Any sinks with an area of less than 0.0495 are removed according to the minimum lake area needed to support potential hydrofracture (Krawczynski et al., 2009; Miles et al., 2017).

After the processing chain is complete, statistics are performed on the outputted shapefiles using the Geopandas package available with Python, producing general information such as the total SL area and area change with time, and SL count. Additionally, the unique identifiers for SLs (defined in step 6) are used to analyse the filling and drainage of individual SLs, producing change in area over each given step in the time-series.

7.4 Input data and algorithm output

The input data is Sentinel 2A and 2B scenes during the summer melt season. No distinction is made between ascending and descending scenes.

The output data consists of vectorised polygons that represent each classified water body.

7.5 Accuracy and performance

The method performs well and the error in the SL count is on the order of +/-15% and slightly higher for the SL area +/-22%. The higher error in the area estimation is due to the impact of lake ice partially covering the surface of some lakes. This is based on a comparison of automatically delineated lakes in a subset test area, to a manually delineated test dataset of the same imagery and is described in ST-DTU-ESA-GISCCI+-E3UB-00.

7.6 Capabilities and known limitations

The band ratio NDWI is a robust method to delineate water bodies on ice and has been applied to a variety of optical imagery in numerous SGL studies, e.g. Yang and Kang (2013), Moussavi et al. (2016), Miles et al. (2017), Williamson et al. (2018). There are some limitations that can affect the results such as ice cover on lakes. Whilst this is not a limitation of the algorithm itself as it is tuned to detect liquid water, the presence of ice cover over some of the lake can therefore lead to an under classification of water body extent. To limit this a dual threshold is used as described in ST-DTU-ESA-GISCCI+-PMP-001. Similarly, saturated snow can lead to an over classification of water bodies, again this is reduced by using the dual threshold.

7.7 References

Feng, M., Sexton, J.O., Channan, S., Townshend, J.R.,(2015). A global, high-resolution (30-m) inland water body dataset for 2000: first results of a topographic–spectral classification algorithm. Int. J. Digit. Earth. https://doi.org/10.1080/17538947.2015.1026420

Feyisa, G.L., Meilby, H., Fensholt, R., Proud, S.R., (2014). Automated Water Extraction In-dex: A new technique for surface water mapping using Landsat imagery. Remote Sens. Environ. 140, 23–35. https://doi.org/10.1016/J.RSE.2013.08.029

Krawczynski, M. J., Behn, M. D., Das, S. B., and Joughin, I. (2009). Constraints on the lake volume required for hydro-fracture through ice sheets. Geophys. Res. Lett. 36, 1–5. doi: 10.1029/2008GL036765

Kääb, A., Winsvold, S., Altena, B., Nuth, C., Nagler, T., Wuite, J., (2016). Glacier Remote Sensing Using Sentinel-2. Part I: Radiometric and Geometric Performance, and Applica-tion to Ice Velocity. Remote Sens. 8, 598. https://doi.org/10.3390/rs8070598

Mankoff et al. in prep High resolution map of Greenland hydrologic outlets, basins, and streams, and a 1979 through 2017 time series of Greenland liquid water runoff for each outlet. Version 1 https://promice.org/PromiceDataPortal/api/download/0f9dc69b-2e3c-43a2-a928-36fbb88d7433

Miles, K. E., Willis, I. C., Benedek, C. L., Williamson, A. G. & Tedesco, M. (2017). Toward Monitoring Surface and Subsurface Lakes on the Greenland Ice Sheet Using Sentinel-1 SAR and Landsat-8 OLI Imagery. Front Earth Sci. Chin. 5, 58

Moussavi, M. S. et al. (2016) Derivation and validation of supraglacial lake volumes on the Greenland Ice Sheet from high-resolution satellite imagery. Remote Sens. Environ. 183, 294–303

Pekel, J.-F., Cottam, A., Gorelick, N., & Belward, A. S. (2016). High-resolution mapping of global surface water and its long-term changes. Nature, 540(7633), 418–422. https://doi.org/10.1038/nature20584

Williamson, A. G., Banwell, A. F., Willis, I. C., Arnold, N. S., (2018). Dual-satellite (Sentinel-2 and Landsat 8) remote sensing of supraglacial lakes in Greenland. Cryosphere, 12, 3045-3065. doi:10.5194/tc-3045-2018.

Yang, K. & Smith, L. C. (2013). Supraglacial Streams on the Greenland Ice Sheet Delineated From Combined Spectral–Shape Information in High-Resolution Satellite Imagery. IEEE Geoscience and Remote Sensing Letters 10, 801–805

Yang, Kang (2019): Supraglacial river and lake analysis. figshare. Software. https://doi.org/10.6084/m9.figshare.9758051.v1

End of document